Contents lists available at ScienceDirect

Heliyon

journal homepage: www.cell.com/heliyon

Research article

Molecular structure, vibrational spectral, electron density analysis on linaloe oil and molecular docking efficacy against the therapeutic target on human immunodeficiency virus-1 organism (VIRAL protein)

Chandramohan Uma maheswari

Department of Physics, Vel Tech High Tech Dr. Rangarajan Dr. Sakunthala Engineering College, Avadi, Chennai, 600062, Tamilnadu, India

ARTICLE INFO

ABSTRACT

Natural traditional medicine extensively uses certain terpenes and gives plants their flavor, aroma, and color. Treatments for bacterial infections, malaria, and cardiovascular disorders, anti-inflammatory, promote circulation, and heal wounds. 3,7-Dimethyl-1,6-octadien-3-ol (Linalool) is a naturally occurring monoterpene alcohol with no cycle and is a colorless liquid. Spectral analysis such as UV absorption spectra, NMR for structure determination, and IR and Raman for vibrational analysis. The Quantum mechanical approach uses DFT, ELF, and LOL-promolecular electron density, non-relaxed, and atomic density analysis. The biomolecular studies such as molecular dynamics using protein-ligand complex with HIV-1 organism (energy minimization). ADMET for the usage of linalool in different metabolism studies and Molecular docking for binding affinity, its reactive site estimation, and macromolecules that come into contact with protein receptors and conclude ligand binding affinity with protein.

1. Introduction

Most naturally occurring compounds are found in plants, the largest and most diverse group is called Terpenes. Natural traditional medicine made extensive use of certain terpenes. They give plants their flavor, aroma, and color. Treatments for bacterial infections, malaria, and cardiovascular disorders, anti-inflammatory, promote circulation, and heal wounds. Terpene shields a variety of living things from abiotic and biotic stressors, including microorganisms, animals, and plants. Nowadays, terpene is used in great quantities in modern medicine for a variety of therapeutic medications. 3,7-Dimethyl-1,6-octadien-3-ol (Linalool) is a naturally occurring monoterpene alcohol with no cycle and colorless liquid. The plant metabolite linalool serves as a volatile oil component, an antibiotic, a fragrance, and a plant metabolite. More than 200 different plant species, including numerous flowering and spice plants, contain linalool. It is the defining perfume of several well-known cosmetic lines and aromas, and it is frequently found in goods that are intended to help people feel calmer. It is present in a variety of fruits, flowers like roses, and spice plants, including ylang-ylang, laurel, tangerine, spearmint, and lemon. In a model of depression, anxiety, and reduced neurogenesis brought on by prolonged corticosterone treatment, rats treated with linalool-rich lavender essential oil showed favorable effects on depressive-type behaviors, enhanced neurogenesis, and dendritic complexity [1]. The knowledge of linalool's antidepressant action mechanisms is highlighted as a new antidepressant phytoremediation [2]. The anti-inflammatory, anti-hyperalgesic, and antinociceptive effects of linalool in different

animal models have been established [3–5]. With both *in vitro* and *in vivo* outcomes, a strong body of data has been built to support the diverse biological features of linalool, with the proof of CNS effects offering the most promising possibility for treating diseases [6]. A significant reduction in the mean xenograft tumor volume and weight was exhibited without an alteration in alanine aminotransferase and aspartate aminotransferase levels in mouse xenografts when mice were fed with 100–200 μg/kg linalool [7]. To emphasize the benefits of a recent line of research on linalool in nanotechnology-based drug delivery systems, which may enable the regular use of linalool as API in the pharmaceutic, cosmetic, and perfumery industries shortly [8]. In this study, spectral analysis like UV absorption spectra to understand the absorption bands, providing information about the variation of bands from the spectra, NMR for structure determination at the atomic level, IR, and Raman for vibrational analysis. With the help of the fundamental laws of quantum physics, versatile tool density functional theory provides a quantitative explanation of material properties is undertaken as the quantum mechanical approach for this compound for understanding the structure through potential energy surface scan for energy description and shape analysis on contrast. IRC enables minimum, maximum, and total energy during the interaction. ADMP for understanding electronic and nuclear kinetic energy. The wave function for the quantitative analysis of molecular surface with minima, maxima of orbital and surface analysis on reactive sites, ELF and LOL-promolecular electron density, non-relaxed and atomic density analysis. The biomolecular studies such as molecular dynamics using protein-ligand complex with HIV-1 organism (energy minimization). The production of molecular dynamics using equilibrium 1 and 2 with energy minimization of protein ligand complex. Progression of hydrogen bond studied during energy minimization through molecular dynamics. ADMET for the usage of linalool in different metabolism studies. Molecular docking for binding affinity and its reactive site estimation. The beneficial in locating bioactive substances that can be utilized to create potent medicines. The results of the above-mentioned approaches will be utilized in prediction *in vivo* and *in vitro* studies.

2. Applied method

The calculations were performed by the DFT (B3LYP/6-31G (d, p)) method (The validity of B3LYP/6–31 G (d, p) density functional theory in investigating geometry optimization and determining geometrical parameters has been demonstrated) [9,10] on 11th Gen Intel(R) Core (TM) i5-1135G7 @ 2.40 GHz, 2419 MHz, 4 Core(s), 8 Logical Processor(s)z personal computer using Gaussian 09 W program package [11]. Harmonic vibrational frequencies were calculated, the frequencies were scaled and the structure was optimized. Selected single-point energy analyses using the PES scan are conducted, and internal coordinates using Gauss view 5.0 8 [12]. Multiwfn, wavefunction analysis, a very comprehensive function method is applied [13]. Molecular dynamics using GROMACS 2022.5 [14] of protein and ligand interaction. ADMET - the internal processes that describe drug movement are calculated [15]. Molecular Docking studies were carried out using the AutoDock suite and the generated configuration from AutoDock by using Vina [16,17] as a docking engine, the output is taken from the executed file (Through the ligand-based virtual screening approach, and the protein will be selected by the ligand for docking). Molecular Dynamics program dart in ubuntu 20.040 version Linux terminal with Linux command program tool (GUI) Gromacs-2022.5 and analyzed protein-ligand interaction using protein Human immunodeficiency virus-1 with 3,7-Dimethyl-1,6-octadien-3-ol [18].

3. Results and discussion

3.1. Molecular geometry

The compound 3,7-Dimethyl-1,6-octadien-3-ol contains $C_{10}H_{18}O$ (29 atoms). From Fig. 1 the combination of carbon-hydrogen shows the bond length range from 1.084 Å-1.1 Å. The combination of carbon-carbon shows the bond length in the range of 1.331 Å −1.554 Å. Due to a negative correlation, the bond energy decreases as the bond length increases. This inverse relation was found between the bond length carbon-carbon to the maximum of 1.554 Å (C_3–C_4) when compared with carbon-hydrogen bonding. This is due to (sp³-s orbital) high electron density overlaps of the C–H bond and (sp³-sp³ orbital) low electron density overlap of the C–C bond.
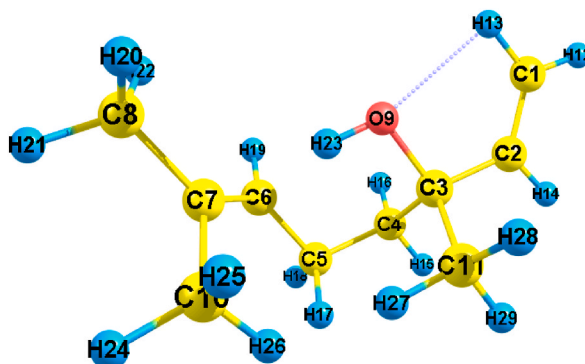

Fig. 1. Atom numbering scheme of 3,7-Dimethyl-1,6-octadien-3-ol.

The bond length of O_9–H_{23} is 0.969 Å, due to oxygen being more highly electronegative than hydrogen atoms. Moreover, oxygen-hydrogen usually gives its bond length in the range of 9.57×10^{-11} m and the double bond length between carbon-oxygen is found about 1.2 Å, and in others, the bonds is 1.43 Å and in our present study the bond length of C_3–O_9 is 1.428 Å, this may be due to stretching of bond length by the O_9–H_{23}. A strong hydrogen bond between O_9 (donor) and H_{13} (acceptor) was formed with a bond distance of 2.291 Å on shortening of the bond distance (O_9–H_{23}) to 0.969 Å shown in Table 1. Magali Benoit and Dominik Marx studied the shape of proton in hydrogen bonds based on bond length, where it showed the spherical shape of the proton which is characterized by proton density distribution of the proton coordinates' quantum uncertainty outcome with stretching along the hydrogen bond axis [19].

3.2. Absorption spectra

The interaction of ultraviolet and visible radiation with matter results in electronic transitions, which are the promotion of electrons from their ground state to a high-energy state. The time-dependent density functional theory manifests as a powerful and effective computational tool for the study of ground and excited state properties. Fig. 2 shows the three absorption spectra approximately at 204 nm, 195 nm, and 188 nm for 3,7-Dimethyl-1,6-octadien-3-ol. The Excitation energy (ΔE), Absorption wavelength (λ), and Oscillatory strength (f) are given in Table 2. Electronic transitions in organic molecules in the vast majority of cases involve transitions of sigma (σ) electrons, n-electrons, and π-electrons [20]. The absorption at 204 nm and 195 nm shows $\pi \rightarrow \pi^*$ bonding orbital to anti-bonding, out of which 204.10 nm shows an intense peak with a longer wavelength (Bathochromic effect). The wavelength at 188 nm shows the $n \rightarrow \sigma^*$ non-bonding orbital to anti-bonding orbital and affirms the presence of the alcohol group with higher energy or shorter wavelength comparatively with other wavelengths. The hydrogen bonding's significant impact on transitions $n \rightarrow \sigma^*$ is confirmed through this by moving towards a shorter wavelength.

3.3. NMR analysis

The Gauge-Independent Atomic Orbital (GIAO) carbon chemical shift calculations for 3,7-Dimethyl-1,6-octadien-3-ol are made, which is a superior approach to exhibit a faster convergence for many aspects at the present state of the subject. The calculation was made by using RB3LYP/6-31G (d, p) NMR = GIAO. The calculated values for 13C NMR are shown in Table 3. The chemical shifts were measured for the solvents DMSO and Chloroform respectively. The accuracy ensures accurate interpretation of spectroscopic parameters when you consider that the range of 13C NMR chemical shift for comparable organic compounds typically is > 100 ppm [21]. In this study, 13C the NMR chemical shift of all carbon atoms falls in the range less than 100 ppm. The factors that control the chemical shift may be due to the geometry of the carbon atom and the electronegativity of other atoms around the carbon atom. The bond angle for the carbon atoms C_2–C_3–C_4, C_2–C_3–O_9, C_2–C_3–C_{11}, C_4–C_3–O9, C_3–C_4–H_{15}, C_3–C_4–H_{15}, C_3–C_4–H_{16}, O_9–C_3–$C11$, C_3–O_9–H_{23},

Table 1
Optimized parameter of 3,7-Dimethyl-1,6-octadien-3-ol.

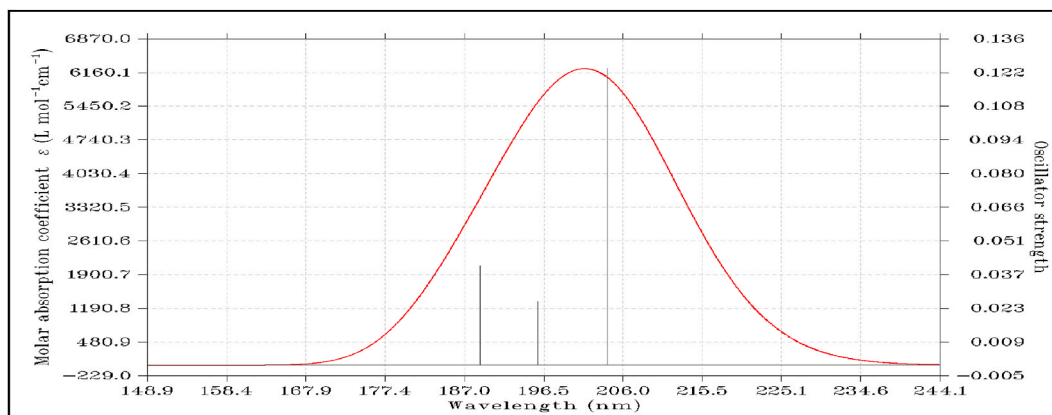| Parameters	Bond Length (Å)	Parameters	Bond Angle (°)	Parameters	Bond Angle (°)
C_1–C_2	1.331	C_2–C_1–H_{12}	121.3	H_{17}–C_5–H_{18}	105.6
C_1–H_{12}	1.086	C_2–C_1–H_{13}	120.9	C_7–C_6–H_{19}	116.9
C_1–H_{13}	1.084	C_1–C_2–C_3	125.3	C_6–C_7–C_8	120.7
C_2–C_3	1.515	C_1–C_2–H_{14}	120.1	C_6–C_7–C_{10}	124.9
C_2–H_{14}	1.09	H_{12}–C_1–H_{13}	117.8	C_8–C_7–C_{10}	114.4
C_3–C_4	1.554	C_3–C_2–H_{14}	114.6	C_7–C_8–H_{20}	111.2
C_3–O_9	1.428	C_2–C_3–C_4	108	C_7–C_8–H_{21}	110.8
C_3–C_{11}	1.543	C_2–C_3–O_9	107.4	C_7–C_8–H_{22}	112
C_4–C_5	1.546	C_2–C_3–C_{11}	108.8	C_7–C_{10}–H_{24}	110.3
C_4–H_{15}	1.097	C_4–C_3–O_9	110.6	C_7–C_{10}–H_{25}	110.7
C_4–H_{16}	1.096	C_4–C_3–C_{11}	112.2	C_7–C_{10}–H_{26}	113.5
C_5–C_6	1.508	C_3–C_4–C_5	116.8	H_{20}–C_8–H_{21}	106.4
C_5–H_{17}	1.094	C_3–C_4–H_{15}	108.6	H_{20}–C_8–H_{22}	108.2
C_5–H_{18}	1.1	C_3–C_4–H_{16}	106.9	H_{21}–C_8–H_{22}	108.1
C_6–C_7	1.346	O_9–C_3–C_{11}	109.7	H_{24}–C_{10}–H_{25}	106.3
C_6–H_{19}	1.091	C_3–O_9–H_{23}	107.2	H_{24}–C_{10}–H_{26}	107.7
C_7–C_8	1.511	C_3–C_{11}–H_{27}	111.2	H_{25}–C_{10}–H_{26}	108.1
C_7–C_{10}	1.509	C_3–C_{11}–H_{28}	109.3	H_{27}–C_{11}–H_{28}	108
C_8–H_{20}	1.098	C_3–C_{11}–H_{29}	111.6	H_{27}–C_{11}–H_{29}	108
C_8–H_{21}	1.098	C_5–C_4–H_{15}	108.2	H_{28}–C_{11}–H_{29}	108.5
C_8–H_{22}	1.093	C_5–C_4–H_{16}	109.3		
O_9–H_{23}	0.969	H_{15}–C_4–H_{16}	106.6		
O_9–H_{13}	2.291	C_4–C_5–C_6	114.4		
C_{10}–H_{24}	1.098	C_4–C_5–H_{17}	110.2		
C_{10}–H_{25}	1.097	C_4–C_5–H_{18}	106.8		
C_{10}–H_{26}	1.091	H_{15}–C_4–H_{16}	106.6		
C_{11}–H_{27}	1.095	C_6–C_5–H_{17}	111.4		
C_{11}–H_{28}	1.093	C_6–C_5–H_{18}	108		
C_{11}–H_{29}	1.096	C_5–C_6–C_7	128.9		
		C_5–C_6–H_{19}	114.1		

Fig. 2. UV spectra of 3,7-Dimethyl-1,6-octadien-3-ol.

Table 2
Excitation energy (ΔE), Absorption wavelength (λ), and Oscillatory strength (f) for 3,7-Dimethyl-1,6-octadien-3-ol calculated at TD-DFT (B3LYP/6-31G (d, p)) method.

S.No.	States	Electronic transition	ΔE (eV)	λ (nm)	f
1.	HOMO (41) -> (44) LUMO	$\pi \rightarrow \pi^*$	6.0746	204.10	0.1232
	HOMO (42) -> (44) LUMO				
	HOMO (43) -> (44) LUMO				
2.	HOMO (41) -> (45) LUMO	$\pi \rightarrow \pi^*$	6.3319	195.81	0.0263
	HOMO (42) -> (44) LUMO				
	HOMO (42) -> (45) LUMO				
	HOMO (43) -> (45) LUMO				
3.	HOMO (41) -> (44) LUMO	$n \rightarrow \sigma^*$	6.5652	188.85	0.0413
	HOMO (42) -> (44) LUMO				
	HOMO (43) -> (45) LUMO				

Table 3
Theoretical 13C isotropic chemical shifts (ppm) for 3,7-Dimethyl-1,6-octadien-3-ol.

S.No.	Atoms	RB3LYP/6-31G (d, p) DiMethylSulfoxide	RB3LYP/6-31G (d, p) Chloroform
1.	C_1	65.416	81.782
2.	C_2	24.589	48.869
3.	C_3	8.652	22.892
4.	C_4	37.262	49.009
5.	C_5	49.350	60.188
6.	C_6	39.105	58.260
7.	C_7	44.790	65.689
8.	C_8	53.405	63.797
9.	C_{10}	55.697	65.783
10.	C_{11}	50.574	60.658

C_3–C_{11}–H_{28}, C_5–C_4–H_{15}, C_5–C_4–H_{15}, C_5–C_4–H_{16}, C_4–C_5–H_{17}, C_4–C_5–H_{18}, H_{15}–C_4–H_{16}, C_6–C_5–H_1, H_{17}–C_5–H_{18}, C_7–C_8–H_{21} C_7–C_{10}–H_{24}, C_7–C_{10}–H_{25}, H_{20}–C_8–H_2, H_{20}–C_8–H_{22}, H_{24}–C_{10}–H_{25}, H_{24}–C_{10}–H_{26}, H_{25}–C_{10}–H_{26}, H_{27}–C_{11}–H_{28}, H_{27}–C_{11}–H_{29}, H_{28}–C_{11}–H_{29}, forms the sp^3 hybridization with 1s orbital and 3p orbital to form new similar orbitals showing the tetrahedral arrangement with a bond angle ranging from 105° to 110° which are quite common in nature, shows NMR peaks (shown in Fig. 3) typically below 80 ppm. From the table, the theoretical 13C isotropic chemical shifts (ppm) for 3,7-Dimethyl-1,6-octadien-3-ol using DMSO and Chloroform as a solvent shows the exact positioning of the carbon atom type. The lowering of the ppm value for C_3 is found in both the solvents and also confirms the hydrogen bonding with H–O ….H impression.

3.4. Vibrational spectral analysis

Figs. 4 and 5 show the experimental and theoretical FT-IR and FT-Raman spectra of the title compound. The 29-atom 3,7-Dimethyl-1,6-octadien-3-ol molecule contains 81 normal modes. Out of which, a few important vibrational wavenumbers alone were discussed in the present study. This molecule is a member of the C_1 symmetry family. To fit the estimated wavenumbers with those of the measured ones, scaling factors are applied. Together with the Reduced masses, Force constants, and computed wavenumbers, the
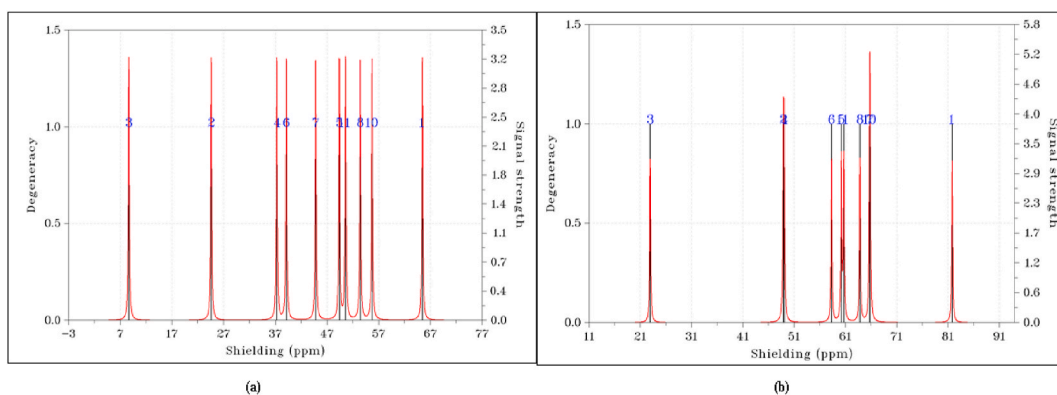
Fig. 3. NMR spectra of 3,7-Dimethyl-1,6-octadien-3-ol using (a) DMSO (b) Chloroform.
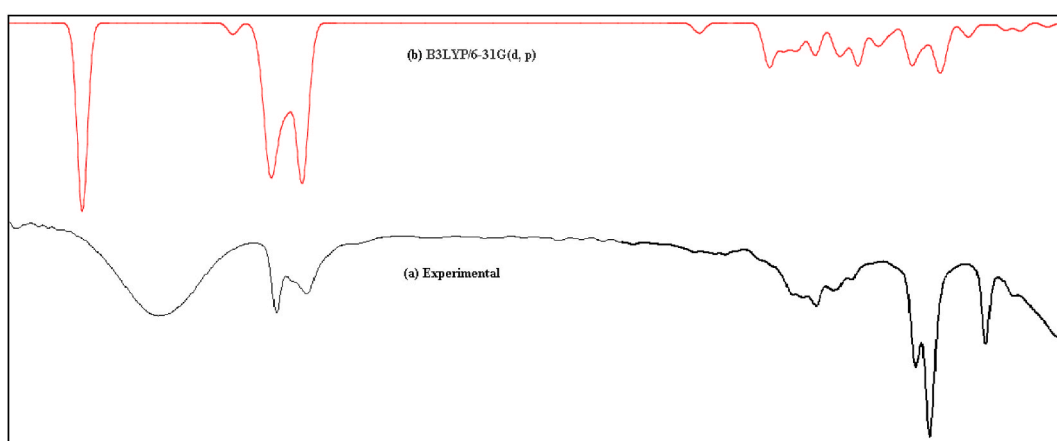
Fig. 4. FT-IR spectra of 3,7-Dimethyl-1,6-octadien-3-ol (a) Experimental (b) B3LYP/6-31G (d,p).
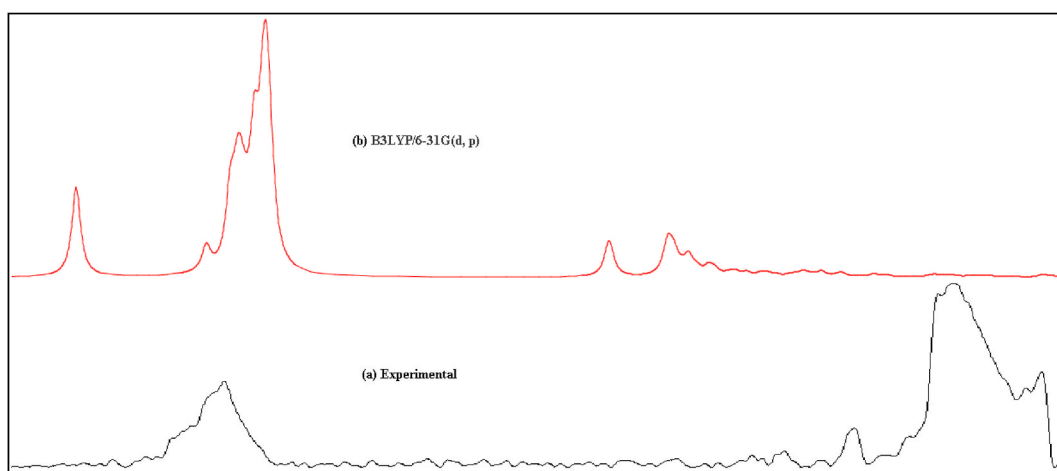
Fig. 5. FT-Raman spectra of 3,7-Dimethyl-1,6-octadien-3-ol (a) Experimental (b) B3LYP/6-31G (d,p).

experimental FT-IR and FT-Raman wavenumbers [22] are reported in Table 4. From this, we can understand that a bond's strength can be determined by the force constant. With increasing bond strength and lowering decreased mass of the bound atoms, the value of the stretching frequency of a bond rises.

Table 4
Vibrational assignment for 3,7-Dimethyl-1,6-octadien-3-ol.

FTIR[a]	FT Raman[a]	Scaled Frequency	IR Intensity	Raman Activity	Reduced Masses	Force Constants	Vibrational Assignment
–	3619	3604	150.31	222.69	1.07	8.84	OH bond
3322	–	3131	9.04	61.00	1.12	6.97	OH bond
2971	–	2977	27.69	27.39	1.09	6.18	CH stretching
2883	–	2895	23.29	108.95	1.07	5.73	CH symmetric stretching
–	1672	1668	4.68	58.27	6.24	11.09	CC stretching
–	1431	1434	2.55	9.86	1.08	1.42	CH$_2$ symmetrical bending
1417	–	1424	3.99	11.22	1.08	1.40	CH$_3$ symmetrical bending
1379	–	1380	1.12	28.42	1.25	1.52	CH$_3$ asymmetric bending
1328	–	1343	9.41	5.43	1.42	1.63	CH$_3$ symmetric bending
–	1314	1307	1.69	6.58	1.28	1.39	CH$_3$ asymmetric bending
1277	–	1280	4.93	14.32	1.31	1.38	OH in-plane bending
–	1185	1207	16.08	12.03	1.64	1.53	COH stretching
1085	–	1094	13.16	9.24	1.96	1.50	CO stretching
1044	–	1060	6.32	5.74	1.62	1.16	CO stretching
879	–	890	1.91	6.85	1.95	0.99	CH bending

[a] [22].

3.4.1. O–H and C–O vibration

Non-hydrogen-bonded OH ions also exhibit a somewhat broad wavenumber range, ranging from 3670 to 3500 cm^{-1}. Strong hydrogen bridges can have wavenumber shifts of up to 3100 cm-1 due to the involvement of OH ions that display much higher wavenumber shifts [23]. In the present study, the OH vibrational mode is found at 3619 cm^{-1} in FT-Raman spectra and this is confirmed by the theoretical analysis at 3604 cm^{-1}. Normally, the broad band of OH alcohol is found between wavenumber between 3200 and 2700 cm^{-1} of intramolecular bonding. The same was found at 3322 cm^{-1} in FT-IR spectra and 3131 cm^{-1} by B3LYP/6-31G (d, p) method. The vibrational assignment for the wavenumber at 1185 cm^{-1} in FT-Raman spectra and 1207 cm^{-1} in gas phase is due to the hydrogen bond generation in the tertiary alcohol has caused it to have a very wide OH tension band with carbon stretching. The added value for these vibrations is provided by the FT-IR peak at 1277 cm^{-1}, which is analyzed as OH in-plane bending. A strong CO stretching is usually found between 1085 and 1050cm-1 and a strong band is found in this present study at 1085 cm^{-1}, 1044 cm^{-1} at FT-IR and this was supported by the gas phase value at 1094 cm^{-1} and 1060 cm^{-1}.

3.4.2. C–H vibration

The CH stretching of alkane with medium peak falls in the region from 3000 to 2840 cm^{-1}, this can be seen from Table 4, where 2971 cm^{-1}, a weak peak at 2883 cm^{-1} in FT-IR and in the gas phase of around 2977 cm^{-1} and 2895 cm^{-1}. A strong trisubstituted CH bending mode occurs at 880 ± 20 cm^{-1}. In this study, the same bending mode occurs at 879 cm^{-1} at FT-IR and 890 cm^{-1} in the gas phase.

3.4.3. C–C vibration

The trisubstituted [24] 3,7-Dimethyl-1,6-octadien-3-ol shows CC weak stretching between 1675 and 1665 cm-1, the same vibration is observed in our study at 1672 cm^{-1} at FT-Raman spectra and 1668 cm^{-1} in the gas phase. As a result, the carbon atom's frequency of vibration decreases, demonstrating an increase in reduced mass.

3.4.4. CH$_2$ and CH$_3$ vibration

In the IR and Raman spectra, the scissoring mode [25] of the CH$_2$ group generates a unique band in 1465 cm^{-1}. This band often crosses over with CH$_3$ anti-symmetrical bends at 1470-1430 cm^{-1}. This encourages the findings in both experimental values at 1431 cm^{-1} in FT-Raman spectra and 1434 cm^{-1} by the B3LYP/6-31G (d, p) method. The rocking, wagging, and twisting appear [25] in the region of 1422–719 cm^{-1}. These vibrations result in weak IR and medium Raman bands for alkanes when they interact with nearby CH$_2$ groups. From the table, FT-IR wavenumbers such as 1417 cm^{-1}, 1379 cm^{-1}, 1328 cm^{-1}, and the wavenumber 1314 cm^{-1} at FT-Raman confirms that the vibrations are CH$_3$ in bending mode which the theoretical data 1424 cm^{-1}, 1380 cm^{-1}, 1343 cm^{-1}, and 1307 cm^{-1} supports.

3.5. Potential energy surface

By allowing representations and modifications to molecules or systems of molecules' shape and geometry to be linked to the electronic energy of the system, the potential energy surface makes it possible to apply Schrödinger's equation to molecules. The potential energy surface (PES), which displays the relationship between a molecule or system of molecules' energy and geometry or coordinates, is one of the essential concepts in computational chemistry. As a result, finding and describing potential energy surfaces has a wide range of applications in computational chemistry. The basic set keywords of 3,7-Dimethyl-1,6-octadien-3-ol (Linalool) in the Gaussian 09 W program were RB3LYP/6-31GSingular-point energy assessments are conducted over a rectangular grid with specific angles as part of a rigid PES scan. The PES 3D displays saddle points of energy as dots, with red being the highest level and blue denoting the lowest level. The 3D diagram of a PES scan performed for the dihedral angles C1, C2, C3, O9, and O9, C3, C5, and C6 at the

B3LYP/3-21G level for the title molecule angles was varied in steps of 20°, 40°, and 360°. The total potential energy values described as minimum, maximum, and end saddle points were mentioned as a, b, and c with an arrow marked and highlighted in red color [26]. Total energy eV figures are as follows: Step 1 (a), Energy = −12707eV, Step 2 (b), Energy = −12706.80eV, and Step 3 (c). Energy = −706.90eV. The observed values shown in the 3D scan Fig. 6 (i), such as those in the a, b, and c stated figures, and the 2D Fig. 6 (ii) arrow mark symbol points each individually indicate the total energy. Gaussian Scan computations across two variables are plotted using Gauss View to create three-dimensional surfaces.

3.5.1. Intrinsic reaction coordinate (IRC)

Quantum chemical analysis and the prediction of chemical reaction mechanisms are two common applications of the IRC approach. The IRC gives a unique connection from a given transition structure to the local minima of the reactant and product sides [27]. This allows for easy understanding of complicated multistep mechanisms as a set of simple elementary reaction steps. A specific option is the intrinsic reaction coordinate (IRC), which is the minimal energy reaction pathway between a reaction's transition state and its reactants and products in mass-weighted cartesian coordinates. According to highlight ("a") in Fig. 7, the IRC minima value one is 0.72931eV and the total energy is −12555.8eV. IRC's second minima are equal to −0.79907eV, with total energy equal to −12555.8eV highlighted "(b)" in Fig. 7. We noticed that the first and second minima values changed in this, but the overall energy remained unchanged, as shown in Fig. 7.

3.6. ADMP

ADMP (Atom-Centered Density Matrix Propagation) approach, where the one-electron density matrix expanded in an atom-centered Gaussian basis set is propagated as electronic variables along with the classical nuclear degrees of freedom via an extended Lagrangian procedure [28]. The ADMP method has appealing characteristics like the ability to accurately treat all electrons or use pseudopotentials to simulate research systems, the ability to use large time steps by using small values for tonsorial fictitious mass, the use of a wide range of accurate and effective exchange-correlation functionals, and hybrid density and kinetic energy functionals. In the simulated dissociation trajectories' analysis in the DEA dissociation process, bonds are broken within femtoseconds of the simulation time scale, and the dissociation trajectory differs depending on the size of the three basis sets. The method is carried out by using the B3LYP functional of density functional theory and the 6–31 + G (d, p) basis sets with the geometry of 3,7-Dimethyl-1, 6-octadien-3-ol. Input data maximum number of steps 50, random number generator seeds 398465, time each step = 0.10000 fs, fictitious electronic mass = 0.10000 amu, MW individual basis function is true, initial nuclear kinetic energy is 0.10000 eV, initial electron kinetic energy = 0.00 eV, Multitime step – NDtrC = 1, Multitime step - NDtrP is no thermostat chosen to control nuclear temperature. A total simulation of 5000 steps is run for each trajectory. Time in femto second of electronic kinetic energy and kcal/mol of nuclear kinetic energy the minimum nuclear kinetic energy is 1.37745eV of time in trajectory (femtosecond) is 5 further details shown in Fig. 8 maximum nuclear kinetic energy is 2.72116eV of time in trajectory is 0 shown Fig. 8. All of the dissociations cannot be given in a finite number of trajectories in our ADMP calculations since no restriction is applied to the dissociation trajectory calculations. The regular ADMP equations are seen to arise in the special case of the $\hbar \to 0$ limit of the current formalism. Semiclassical approximations are also discussed, and rigorous error estimates are provided to define the accuracy of the current formalism [29]. Low-energy electrons can connect to biological systems in resonance, but they can also cause dissociation, including processes known as dissociation electron attachment (DEA), which fragments biological systems into neutral molecules. This approach to addressing chemically reactive systems might be precise and effective.

3.7. Wave function

Electronic qualities that are sufficient for predicting bioactivity can be determined using wavefunction-dependent features such as QAM-surface, LOL, ELF, PED, and RDG studies. The computation of wave function overlaps for various wave function expansions,

(i) 3D Scan   (ii) 2D Scan
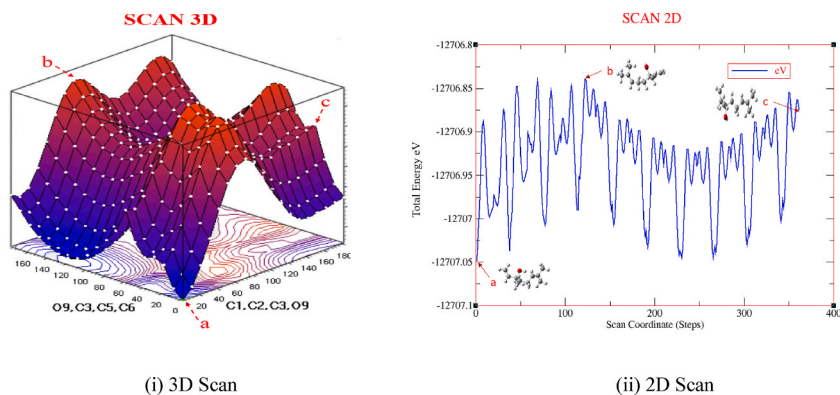
Fig. 6. Potential energy surface (scan).
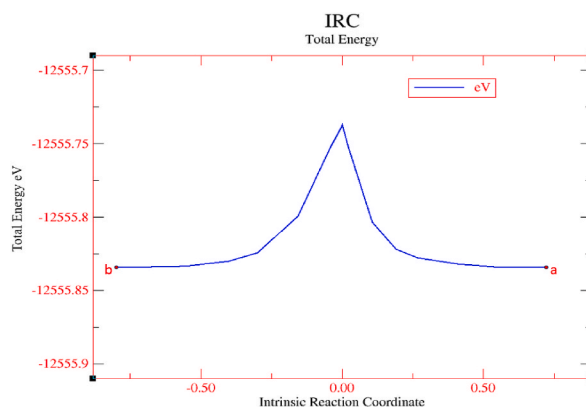
Fig. 7. IRC total energy.
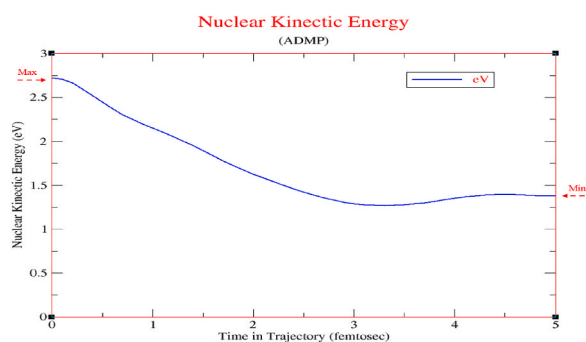
Fig. 8. Nuclear kinetic energy and time in trajectory.

molecular orbitals, basis sets, and molecular geometries is done concurrently using a flexible formalism. The key conclusions are stated in a series of lemmas, corollaries, and theorems that are satisfied by the zeros of the real and imaginary sections of the wave functions on the real line. The wave function ψ may be positive, negative, or imaginary. This $[ψ]^2$ is known as probability density and determines the probability of finding an electron at a point within the atom. We run the wave function program output and parameters defined by three atoms of the H_{24}, O_9, and H_{12} atoms [30]. Wave function used to analyze quantitative analysis of molecular surfaces [see Fig. 9] and show atom labels, reference point, and the contour line corresponding to vdW surface (rho = 0.001) shown in Figs. 10 and 11 compared and confirmed molecular structure and highlighted reference bonds in block color fonts this graph of 3,7-Dimethyl-1,6-octadien-3-ol (Linalool).

Fig. 9. Minima and maxima position.

1. Showing atom labels and reference point
2. showing the contour line corresponding to vdW surface (rho=0.001)

Fig. 10. Electron localization function (ELF).

1. Showing atom labels and reference point
2. showing the contour line corresponding to vdW surface (rho=0.001)
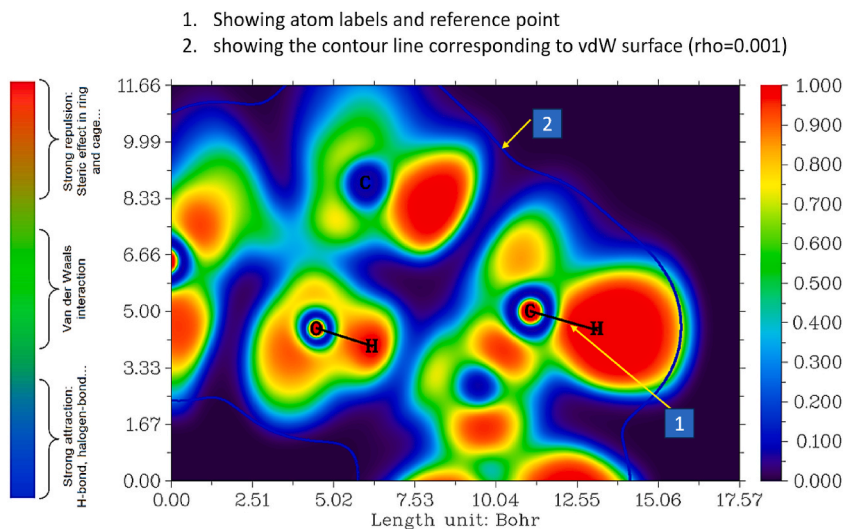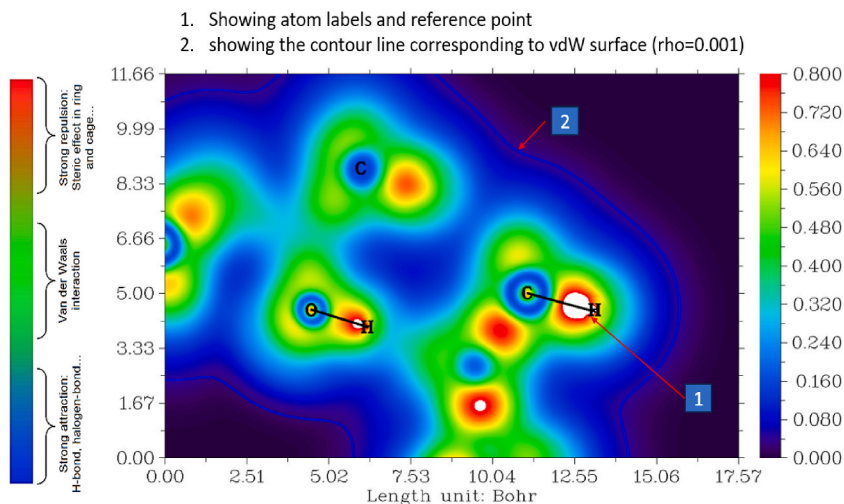
Fig. 11. Localized orbital locator (LOL).

3.7.1. Quantitative analysis of molecular surface (minima and maxima)

A strong technique for predicting reactive sites, molecular characteristics, and intermolecular weak interactions, quantitative analysis of molecular surfaces has many other useful uses as well. Maxima and minima are the main discoveries in a set of lemmas, corollaries, and theorems that are satisfied by the zeros of the real and predictive sections of the wave functions on the real line. The interlacing of these zeros is specifically shown to guarantee that the pertinent probability densities (x) are never null [30] and show a variety of maxima and minima. Details on the minima and maximum of the blue and red color dots, as well as their observed maxima and minima, are shown in Fig. 9, together with their orbital and surface para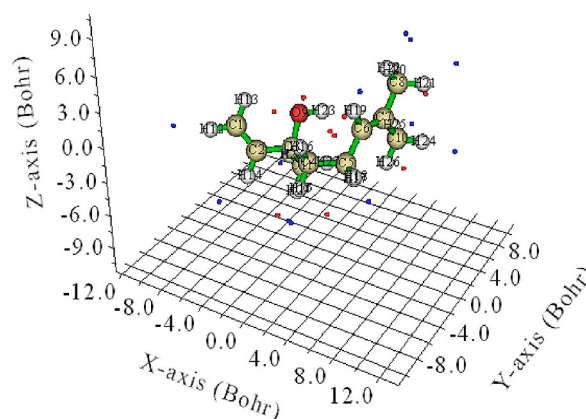meters in Table 5. Additionally, the x-axis Bohr ranges are −12.0, −8.0, −4.0, 0,12,8,4, while the y-axis Bohr ranges are 9.0,6.0,3.0,0.0,3.0,6.0,9.0. Details on other parameters and the orbital minima and maxima positions of the 3,7-Dimethyl-1,6-octadien-3-ol molecules are also provided in Fig. 9, a quantitative evaluation of the molecular surface. Surface characteristics include enclosed volume, average value, standard, total, positive, negative, polar, and non-polar surface area. Individual photon strikes on the screen are represented as dots in the wave function. At the regions where the interference pattern would ultimately be the strongest, a high dot density is anticipated. Stated otherwise, the square of the total electric field at a given position on the screen represents the likelihood (per unit area) that a single photon would strike that region.

3.7.2. Electron Localization Function (ELF) and localized orbital locator (LOL)

Contour maps and ELF, LOL were used to explain the 3,7-Dimethyl-1,6-octadien-3-ol molecule's chemical implications. Multiwfn program executes the ELF and LOL. To identify the locations of bond pairs, lone pairs, and the size of the bonding title molecule, ELF

Table 5
Minima and Maxima of orbital and surface parameters.

Geometry Structure (Orbital Info)						Number of surface minima: 13 (blue color)						
No.	Atom	Charge	Bohr			No.	a.u.	eV	Kcal/mol	X/Y/Z coordinate(Å)		
			X	Y	Z					X	Y	Z
1	C	6.00	−5.0648	−3.8084	0.5788	1	8.1355	221.3779	5105.1013	−4.8386	−3.5122	0.4221
2	C	6.00	−3.2519	−3.7304	−1.1627	2	9.6939	263.7836	6082.9999	−2.4760	−3.7956	−2.2723
3	C	6.00	−1.0255	−1.9312	−1.1517	3	9.9266	270.1155	6229.0167	−2.4504	1.0479	−3.0404
4	C	6.00	1.4284	−3.5219	−0.8856	4	9.9115	269.7050	6219.5505	−0.8208	−0.9419	−4.3308
5	C	6.00	3.9581	−2.0651	−0.9756	5	11.0323	300.2051	6922.9010	0.9229	−3.8281	1.1275
6	C	6.00	4.3436	−0.2445	1.1834	6	10.5122	286.0507	6596.4918	1.1799	−3.9810	−1.9342
7	C	6.00	5.0220	2.2053	1.1068	7	8.9954	244.7762	5644.6783	2.3360	4.1595	2.7723
8	C	6.00	5.3897	3.6906	3.5171	8	9.4174	256.2594	5909.4868	2.4835	4.3277	−1.2748
9	O	8.00	−1.3263	−0.2891	0.9676	9	11.0045	299.4479	6905.4391	2.7402	−1.2118	2.9343
10	C	6.00	5.5267	3.6868	−1.2776	10	9.1198	248.1624	5722.7659	3.1865	1.8625	4.1949
11	C	6.00	−1.0638	−0.3724	−3.6149	11	10.0651	273.8860	6315.9671	4.0873	−2.8471	−0.6311
12	H	1.00	−6.6105	−5.1519	0.4475	12	8.5228	231.9164	5348.1253	4.9451	3.1365	2.7676
13	H	1.00	−5.0484	−2.5239	2.1750	13	8.8539	240.9271	5555.9154	5.1454	3.1646	−1.2650
14	H	1.00	−3.2949	−5.0309	−2.7593	**Number of surface Maxima: 9 (Red color)**						
15	H	1.00	1.4534	−4.9550	−2.3838	No.	a.u.	eV	Kcal/mol	X/Y/Z coordinate(Å)		
16	H	1.00	1.2894	4.5455	−0.9104					X	Y	Z
17	H	1.00	4.1736	−1.1228	−2.8028	1	13.3478	363.2114	8375.8619	−2.3983	0.5299	0.2014
18	H	1.00	5.4727	3.4868	−0.8965	2	11.9239	324.4658	7482.3668	−0.2511	−2.7340	−2.7983
19	H	1.00	4.0751	−1.0817	3.0490	3	14.2830	388.6613	8962.7510	0.1464	−1.2011	1.9644
20	H	1.00	4.1532	5.3554	3.5681	4	14.4176	392.3235	9047.2034	0.3831	1.8788	−0.3185
21	H	1.00	7.3338	4.4022	3.6563	5	12.6098	343.1291	7912.7530	1.4269	−1.4915	−2.9094
22	H	1.00	5.0030	2.5497	5.1952	6	12.3247	335.3730	7733.8914	2.1029	−2.4493	1.6452
23	H	1.00	0.2085	0.6995	1.1097	7	12.3281	335.4660	7736.0361	2.2960	−2.4632	1.5129
24	H	1.00	7.4958	4.3387	−1.3170	8	10.5055	285.8695	6592.3140	3.2810	3.9360	0.5813
25	H	1.00	4.3476	5.3914	−1.3453	9	12.6176	343.3420	7917.6619	4.2730	−0.1153	−0.5891
26	H	1.00	5.1900	2.6078	−3.0023							
27	H	1.00	0.4751	1.0096	−3.6495							
28	H	1.00	−2.8500	0.6561	−3.7460							
29	H	1.00	−0.8760	−1.5803	−5.2860							

and LOL tools are helpful. The electron density charge distribution is revealed by the ELF and LOL color maps [31]. Figs. 10 and 11 show the two-dimensional color shade maps of the LOL and ELF, respectively. In the ELF map, between 0.0 and 1.0 the color red denotes the highest limit of the ELF scale (1.0), while the color yellow to green denotes the middle ELF scale (0.5), the color blue denotes the lower limit of the ELF scale, and the color black denotes the starting point. Completely delocalized electron locations are shown in the color map by a smaller value of ELF (0.5), whilst non-bonding and bonding localized electron regions are shown by a larger value of ELF (ELF = 1.0). LOL values only go up to a maximum of 0.800. In Fig. 11 the hydrogen atom is surrounded by high ELF areas, indicating a strong localization of both bonding and non-bonding electrons. The blue area surrounding the oxygen and carbon atoms indicates the presence of a delocalization of covalent regions between the carbon and carbon atoms and hydrogen atoms, which is symbolized by a red color with a high LOL value, which may be seen in Fig. 11. The ELF end of the plane at x = −6.70492, y = −8.27663, and z = 7.69911Bohr, and the ELF origin electron plane at x = 2.71739, y = 6.73219, and z = −3.72664Bohr. The one-vector electron localization x = −0.07632, y = −0.03810, z = 0.02279Bohr, and normal value is 0.08829Bohr, and the two-vector electron localization x = − 0.02897, y = −0.03732, z = − 0.03463Bohr and normal value is 0.05858Bohr are observed. The Minimum electron value is 9.001367E-30 and the maximum electron value is 0.9999973. The input index of three atoms is H_{24}, O_9, and, H_{12} yet the minimum and maximum electron values merely differ in that the minimum electron value. LOL Origin value, end plane value, one vector, and second vector value same as ELF but minimum energy and maximum energy values are different. The minimum LOL energy value is 7.499794E-09 and the maximum LOL electron value is 0.971334. Strong attraction H-bond, halogen-bond blue to green, van der Waals interaction show color green, strong repulsion steric effect in ring or atoms yellow to red color. The blue color border line showing in ELF and LOL of the wave function is the contour border line corresponding to the vdW surface (rho = 0.001) shown in Figs. 10 and 11.

3.7.3. Reduced density gradient (RDG)

Non-covalent interactions (NCI) are a visualization index that is based on the density and its derivatives. These derivatives make it possible to recognize non-covalent interactions. It is predicated on the peaks that show up at low densities in the reduced density gradient (RDG). Because the density gradient is annihilated at these critical places between molecules, there is a significant change in the RDG at these locations. The development of steep peaks at low density is the primary distinction between the monomer and dimer situations when we plot the RDG as a function of density throughout a molecule [32]. A scalar field of the electron density is the reduced density gradient (s), which is defined as

$$s(r) = \frac{|\nabla \rho(r)|}{2(3\pi^2)^{1/3}\rho(r)^{4/3}}$$

Strong, alluring encounters are indicated by blue. RDG can reconstruct the entire electronic pairing distribution; core, lone pairs, and interatomic bonding regions appear as minima of RDG. Red denotes substantial non-bonded overlap. This RDG output of 29 atom molecules with 28 bonds, a minimum range of 0.0309, and an observed grid size of 115 × 68 × 68 showed a total of 531760 (voxels) grid points per side. Bonded ($\lambda_2 < 0$) and non-bonded ($\lambda_2 > 0$) materials can be identified by their λ sign. The RDG analysis findings plotted by the Multiwfn 3.8 package and (https://www.ks.uiuc.edu/Development/Download/download.cgi?PackageName=VMD).

VMD (1.9.4) programs are displayed in Fig. 12 to help clarify the nature of the intermolecular interaction of 3,7-Dimethyl-1,6-octadien-3-ol. There are numerous spikes are observed in the scatterplot showing in the range from −0.05 to +0.05 a.u. To examine the weak, strong, and strong repulsion interactions of the molecule under study, a reduced density gradient (RDG) was also shown. Positive values of sign (λ_2) ρ (right side of Fig. 13) suggest strong repulsive interactions (steric effect), whereas negative values of sign (λ_2) ρ (left side of Fig. 13) imply attractive interactions with the other molecule. The van der Waals interactions and steric effects are used to portray strong hydrogen bonds in the intermolecular interactions of 3,7-Dimethyl-1,6-octadien-3-ol molecules with reduced density gradient (RDG) in a colorful graphic. The RDG isosurface for 3,7-Dimethyl-1,6-octadien-3-ol reveals a significant van der Waals contact. The system that produces the steric effect is reflected in the red color, which represents the intensity of the molecular structure; blue indicates stronger attraction. To reflect the interaction between van der Waals, this reaction was exhibited in a green color [32–34].
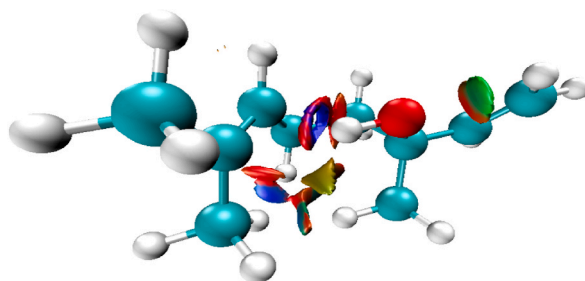

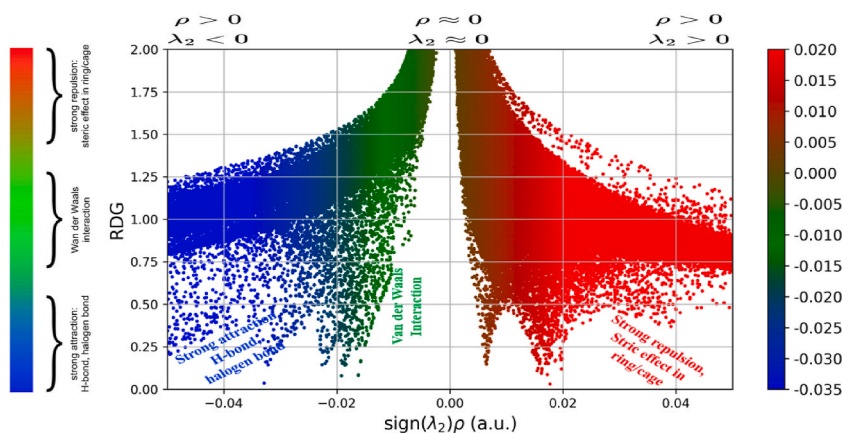**Fig. 12.** Non-covalent interactions structure view.

Fig. 13. Reduced Density Gradient Gnu-plot scatter graph (RDG).

3.8. Molecular dynamics of protein-ligand complex

MD simulations are uniquely suited for examining the structures of membrane-associated protein-ligand complexes with atomistic detail [35]. Using molecular dynamics (MD) simulations, the mechanism and dynamic stability of the interaction between linaloe oil and HIV-1 were determined [36]. Molecular Dynamics tool Gromacs 2022.5 version used and analyzed protein Human immunodeficiency virus-1 organism and Viral Protein of RCSB ID 1QR9 and Resolution: 1.60 Å (https://www.rcsb.org/structure/1QR9) with ligand Dimethyl-1,6-octadien-3-ol drug. Gromacs 2022.5 version Program run steps are shown in Fig. 14 [37]. (Gromacs) Production of Molecular Dynamics of Configuration of Gromacs nsteps = 500000; * 5000000 = 10000 ps (10 ns), constraint algorithm = lincs, holonomic constraints, protein in water, ligand and hydrogen bond pairs within 0.35 nm". The energy minimization of the system was carried out using the steepest descent algorithm with maximum steps of 50,000 both for the predicted protein structure and the template protein structure, where the consideration of tolerance was 1000 kJ mol $^{-1}$ nm $^{-1}$. After system minimization, it was equilibrated at both canonical ensemble (NVT) and isothermal–isobaric ensemble (NPT) for 100 ps. After molecular dynamics were generated [38], we analyzed protein, residues, and water and split them into groups. Completion of molecular dynamics production RMSF, RMSD, Gyrate, hydrogen bond, and protein with ligand interaction graphs were generated in XMgrace (Grace Home (weizmann.ac.il)) Fig. 14. The Particle Mesh Ewald (PME) summation was used for long-range electrostatic interactions with a PME order. The Linear Constraint Solver (LINCS) algorithm was applied to constrain the bonds containing hydrogen atoms, and the settle algorithm was used to constrain the geometry of water molecules. The application of the V-rescale weak coupling method
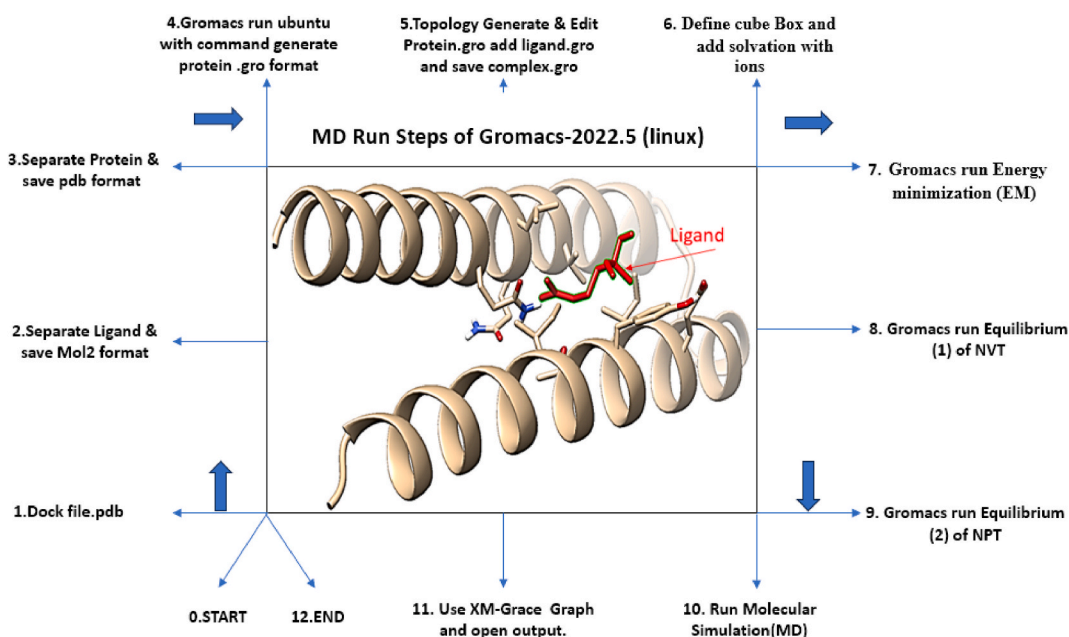

Fig. 14. Molecular dynamics of HIV protein & ligand Gromacs (Linux) steps.

regulated the temperature at 300 K, whereas continuous maintenance of pressure at 1 atom (1.01325 bar) was modulated by the method. The LINCS algorithm and a 2 fs (fs) integration step were used for the 100 ns MD run production with no restraints [39].

3.8.1. Potential energy of the solvated system

The GROMACS Energies (potential) has the headings "Time (ps)" and " (kJ/mol)" on the x and y axes, respectively [37]. The initial potential energy is 0.000000 ps and −297856.062500 kJ/mol (-5e+6), the ending potential energy is 416.000000ps and −446057.406250 kJ/mol, and the mean potential energy is 176.000000ps and −435233.437500 kJ/mol, as illustrated shown in xm-grace graph Fig. 15(a) and the energy minimization step has an impact on this. Only when the potential energy function closely resembles the forces that "real" atoms feel will simulation results be realistic.

3.8.2. Radius of gyration

The extent of the major protease's gyration, both overall and around the axes. Gyrational radius is shown on the Y axis in angstroms, while simulation duration is shown on the X axis in picoseconds. A popular metric for assessing how compact protein molecules are in Rg. Lower values of Rg correspond to a more folded or compact structure, while higher values indicate more stretched or flexible conformations during simulation [37]. Gyrate plot details are provided in Fig. 15(b) with the starting value of 0.0ps, Rg being 1.59430 nm, RgsX being 1.52351 nm, RgsY being 1.51681 nm, and RgsZ being 0.679563 nm, and the end of the gyration being 10000ps time Rg being 1.59430 nm, RgsX being 1.48519 nm, RgsY being 1.50633 nm, and RgsZ being 0.676048 nm. The simulated protein structure's gyration radius as well as gyration radii about the x, y, and z axes as a function of time were calculated using the 'gmx gyrate' function. The equilibrium conformation of the entire system was described using the parameter Rg (Fig. 15(b)).

3.8.3. Root means square deviation (RMSD)

The difference between a protein's backbones from its initial structural conformation to its final position is measured using the RMSD formula. The variations generated during the simulation of the protein can be used to gauge its stability concerning its conformation. The plot shows all the atoms in the residues of the binding site [37]. While the X-axis displays simulation duration in nanoseconds, the Y-axis displays the RMSD of binding site residues. The RMSD is 0.5043727 nm, the minimum time is 0.0000000 ns, and the maximum duration is 10.0000000 ns with an RMSD of 1.4205656 nm. Details are provided in Fig. 15(c) including the meantime value of 5.0000000ns and the mean nm value of 1.0388827 nm. RMSD indicates positional variations over time between complete structures.

3.8.4. Root mean square fluctuation (RMSF)

The difference between the backbones of a protein from its initial structural conformation to its final position is measured using the root mean square deviation (RMSF). The variations generated during the simulation of the protein can be used to gauge its stability concerning its conformation. A residue's flexibility, or how much it moves or changes during a simulation, is calculated using the RMSF formula [37]. The RMSF starting plot range is given in Fig. 15(d) as x-axis label atom 1, y-axis label nm is 0.4398 nm, and the final value of the plot is x-axis atoms = 1088 and y-axis = 0.2741 nm. When plotted against the number of residues, RMSF per residue can reveal which amino acids in a protein structurally contribute the most to molecular motion.

3.8.5. Hydrogen bond and interaction analysis of protein with ligand

The progression of all hydrogen bonds between the primary protease. The geometry alone is used by the gmx H-bond module to determine the hydrogen bonding. More specifically, two cutoffs serve as the foundation for the H-bond interactions between two groups: the angle formed by the three atoms in a hydrogen bond, Dn, and H- the separation between the two heavy interacting atoms (Ac-Dn) [39]. Following a molecular simulation, the command "gmx hbond -s em.tpr -f md_0_10_center.xtc -n index. ndx -num hbond. xvg" was run in Gromacs Linux. The ligand (3,7-Dimethyl-1,6-octadien-3-ol) and protein (1QR9) were picked from group 1 and group 13, respectively. The hydrogen bond graph in Fig. 15(e) was output plotted using a graph by the XM grace tool. The GROMACS hydrogen bond x-axis has the label "Time (ps)" and the y-axis has the label "Number." The hydrogen bond time x-axis starts at 0.0ps and the atom number y-axis is 0–61 and 363 nm (Pairs within 0.35 nm) and ends at 10000ps and the atom number y-axis is 62–61 and 355 nm (Pairs within 0.85 nm), respectively. The Interaction between protein and ligand command "gmx energy -f ie. edr -o interaction_energy.xvg" in the Gromacs GUI program used to study the interaction between protein and ligand was employed, and the output was seen in the XMgrace support analysis output plot given in Fig. 15(f). "Time (ps)" is written on the x-axis, and " (kJ/mol)" is written on the y-axis [39]. The x-axis's initial value range is 0.00ps, while the y-axis's value is −44.193138 kJ/mol. The x-axis's final interaction value range is 10000ps, while the y-axis's value is −25.016916 kJ/mol. This gives the non-bonded interaction between the protein and the ligand. From the interaction, it is observed that the Coulombic and Lennard-Jones (short-range energy) is −50.427860 kJ/mol. The kinetic energy = 7.28521e+04 kJ/mol, pressure (bar) = −1.47126e+02 kJ/mol, RMSD = 2.78852e-06 kJ/mol, Total energy = −3.08718e+05 kJ/mol of LJ-SR: Protein-LIG interaction. In the discipline of biophysics, molecular dynamics (MD) simulation is a potent computer technique used to examine the atomic-level behavior of biological molecules. It offers insightful information about the dynamics and interactions of proteins and their ligands, illuminating important biological processes such as enzymatic reactions, protein folding, and protein-ligand binding. These methods work well for evaluating the structural characteristics of protein complexes with ligands. When used with docking, MD simulation approaches offer a strong complementary relationship [39].
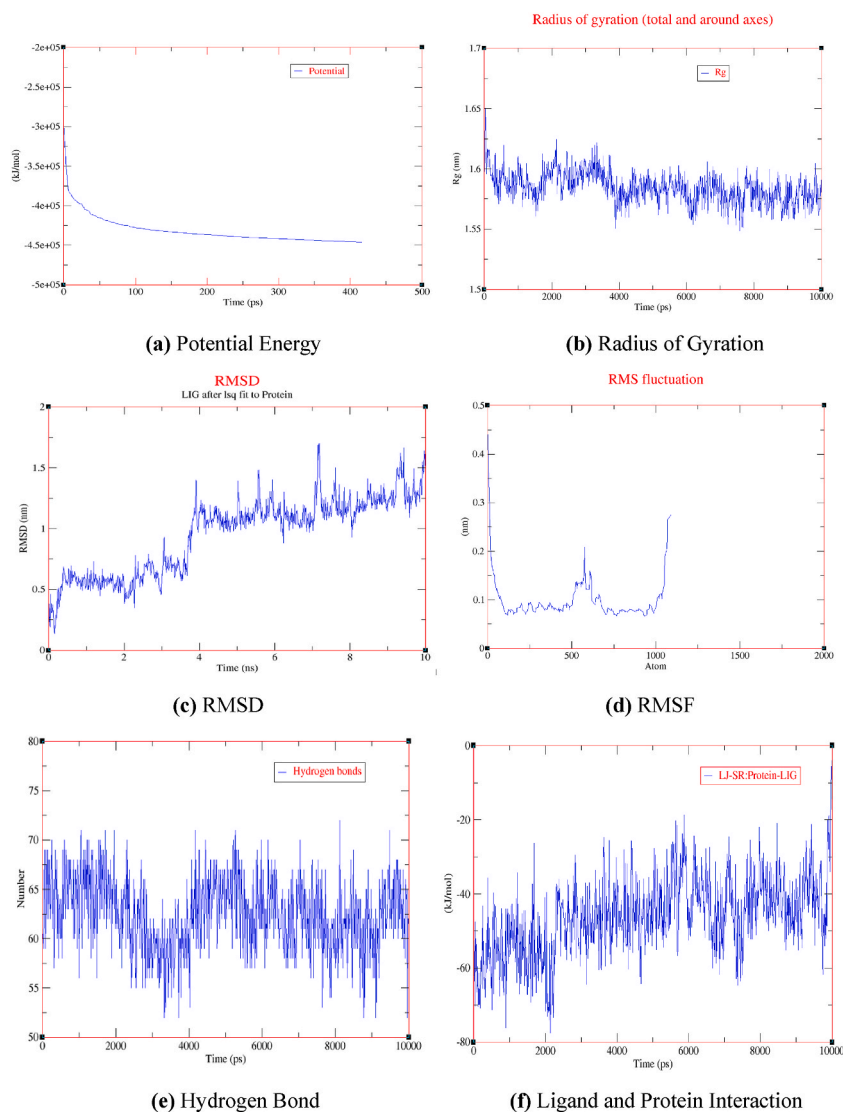
(a) Potential Energy

(b) Radius of Gyration

(c) RMSD

(d) RMSF

(e) Hydrogen Bond

(f) Ligand and Protein Interaction

Fig. 15. Molecular dynamics of HIV protein & ligand.

3.9. ADMET

Drug-likeness, which includes characteristics related to toxicity, excretion, metabolism, distribution, and absorption, is important in the early stages of drug discovery. However, *in vitro* potency is still the main emphasis of current lead optimization efforts, which may result in "molecular obesity" (poor ADMET characteristics). Thus, improving ADMET's characteristics would be a better addition to drug research [40]. Chemical absorption, distribution, metabolism, excretion, and toxicity (ADMET), play key roles in drug discovery and development. A high-quality drug candidate should not only have sufficient efficacy against the therapeutic target but also show appropriate ADMET properties at a therapeutic dose. A lot of in silico models are hence developed for the prediction of chemical ADMET properties. However, it is still not easy to evaluate the drug-likeness of compounds in terms of so many ADMET properties. ADMET details described from the AdmetSAR webserver of 3,7-Dimethyl-1,6-octadien-3-ol drug and provides the latest and most comprehensive manually curated data for diverse chemicals associated with known Absorption, Distribution, Metabolism, Excretion, and Toxicity (ADMET) properties. This ADMET helps to play key roles in the discovery/development of drugs, pesticides, food additives, consumer products, and industrial chemicals. We mention the ADMET property of 3,7-Dimethyl-1,6-octadien-3-ol drug details in Table 6. This information is especially useful when conducting environmental and human hazard assessments. The most critical rate-limiting step in the chemical safety assessment workflow is the availability of high-quality data from the ADMET [41] web server (AdmetSAR 2.0). First, the SMILES of the constituents were obtained using PubChem, an online chemical database. These SMILES were then used to predict the various parameters of the compounds using ADMETL ab 2.0, which gave results about the constituent's physicochemical properties, medicinal chemistry, absorption, distribution, metabolism, excretion, and toxicity parameters. Then the

Table 6

ADMET properties of 3,7-Dimethyl-1,6-octadien-3-ol.

Absorption, Distribution, Metabolism, Excretion and Toxicity		
ADMET Predicted profiles - Classification		
Model	**Result Absorption**	**Probability**
Blood-Brain Barrier	BBB+	0.9699
Human Intentional absorption	HIA+	0.9741
Caco-2	Permeability	0.7201
P-glycoprotein Substrate	Substrate	0.5000
P-glycoprotein Inhibitor	Non- Inhibitor	0.6469
	Non- Inhibitor	0.8311
Renal organic Cation Transporter	Non- Inhibitor	0.9006
Distribution		
Subcellular Localization	Lysosome	0.3689
Metabolism		
CYP450 2C9 Substrate	Non-Substrate	0.8607
CYP450 2C6 Substrate	Non-Substrate	0.8556
CYP450 3A4 Substrate	Substrate	0.5648
CYP450 1A2 Inhibitor	Non- Inhibitor	0.7566
CYP450 2C9 Inhibitor	Non- Inhibitor	0.8385
CYP450 2D6 Inhibitor	Non- Inhibitor	0.9355
CYP450 2C19 Inhibitor	Non- Inhibitor	0.8080
CYP450 3A4 Inhibitor	Non- Inhibitor	0.8309
CYP Inhibitory Promiscuity	Low CYP Inhibitory Promiscuity	0.8199
Excretion Toxicity		
Human ether -a-go-go-related Gene	weak Inhibitor	0.9163
Inhibition	Non- Inhibitor	0.8963
AMES toxicity	Non-AMES toxic	0.9132
Carcinogens	Non - Carcinogens	0.5721
Fish toxicity	High FHMT	0.7883
Tetrahymena pyriformis toxicity	Low TPT	0.6206
Honey Bee Toxicity	High HBT	0.8395
Biodegradation	Ready Biodegradable	0.7291
Acute Oral Toxicity	III	0.8335
Carcinogenicity	Non - required	0.6315

molecules were screened in PASS Online, an online activity predictor, which indicated that 5 of the constituents were mainly anti-eczemic in their activity, with the remaining constituents showing mainly carminative activity and also some antineoplastic activity [42]. By importing the SMILES to the ADMET Lab application, ADMET properties will be predicted. The ADMET property table (value is the predicted label) includes endpoint, value, and probability, respectively. For example, for toxicity endpoints, the value "+" means Positive/Toxic while "-" means Negative/Nontoxic [43–45].

3.9.1. Molecular docking

A method called "molecular docking" uses the atomic-level binding mechanisms of small or large molecules that come into contact with protein receptors and conclude ligand binding affinity with protein [46]. Molecular Docking studies were carried out using the AutoDock suite and on the protein Human immunodeficiency virus-1 organism (Viral -Protein) with ligand Dimethyl-1, 6-octadien-3-ol. The common protein ID No: 1QR9 of the RCSB web server [47]. Discovery visualizer software [48] is used to analyze binding affinity, and interactions and predict conventional hydrogen bond interaction, Alkyl hydrophobic and mixed PI-Alkyl hydrophobic interactions bond, and the function of amino acid groups. We conclude the protein Chain: A acids interact with the Dimethyl-1,6-octadien-3-ol ligand. Protein chain A amino acids interacted with the VAL:25, LEU:21, ILE:48, ILE:55, and TYR:51amino groups performed as Hydrophobic Alkyl and Pi-Alkyl and GLN:18, amino acid groups interacting with the oxygen of ligand as hydrogen bond and unfavorable bump, van der waals of protein groups [49] GLN:22, GLU:47, THR:52, present in docking and the complete details are shown in Fig. 16(a) and (b). The hydrogen bond surface donor color is shown in violet and the acceptor color is shown as green Fig. 16(c) SAS surface blue color range of 25.0,22.5,20 and 17.5, and green color range of 15.0,12.5,10.0 are shown. These two solid surfaces shown white color is neutral Fig. 16(d) and Surface wire mesh volume 8.155,44 area 234,084 probe radius 1.4 and position of surface is x = 1,64761, y = 23,635, z = −53,5419 and the corresponding transparency level is 0.75. After docking protein group list 1) Backbone = 343, Sidechain = 350, Hydrophobic = 20, neutral = 17, Hydrophilic = 31, acidic = 7, basic = 8, Buried = 1, Exposed = 60, ligand = 1, Interface atoms chain:A = 1090, interface ligand = 29, inter pocket atoms = 12, interacting receptor atoms = 6.Docking best Binding affinity −5.0, UFF value 118.54 kcal/mol, docking rmsd lower value and upper value described in Table 7 and [50].

3.9.2. GMX_MMPBSA -protein with ligand interaction

A new tool, gmx_MMPBSA, was used to determine end-state free energy using GROMACS molecular dynamics trajectories. Different configurations were tried against different benchmarks to identify the best possible accuracy [51]. The outcome of Molecular
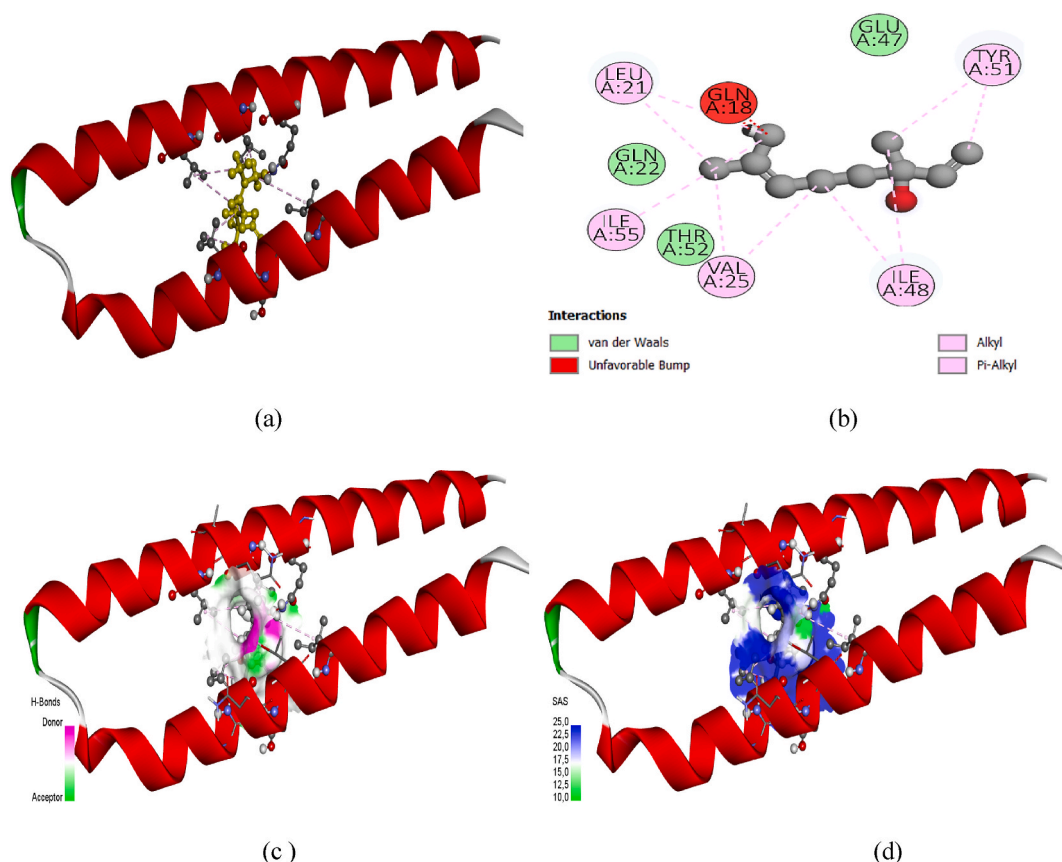
Fig. 16. Docking interaction and all surfaces.

Table 7
Docking best affinity of protein 1QR9 and Dimethyl-1,6-octadien-3-ol.

Ligand	UFF (kcal/mol)	Exhaustiveness = 8 Grid center: x = −30.00, y = 5.31, z = −13.67									Best ligand pose kcal/mol
		Protein: 1QR9	1	2	3	4	5	6	7	8	
Dimethyl-1,6-octadien-3-ol	118.54	Binding Affinity kcal/mol	−5.0	−4.5	−4.5	−4.4	−4.4	−4.3	−4.3	−4.1	−5.0
		RMSD/Upper Bound (Å)	0	2.11	2.4	4.54	14.6	16.06	10.81	12.37	–
		RMSD/Lower Bound (Å)	0	1.54	1.6	2.74	13.2	14.42	7.37	10.39	–

dynamics was used in Linux command program with Python, Amber Tool 2023 with Gromacs 2022.5 GUI-version, and gmx_MMPBSA on 3,7-Dimethyl-1,6-octadien-3-ol, and 1QR9 protein GMX_MMPBSA dat. file for MMPBSA. Three membrane-bound and six soluble protein systems make up the benchmark in this work. The user has the option to do binding free energy calculations with several solvation models (PB, GB, or 3D-RISM) in addition to stability calculations, computational alanine scanning, entropy corrections, and binding free energy decomposition using gmx_MMPBSA. One may accurately and swiftly predict the free energy of ligand binding using the gmx_MMPBSA/PB(GB)SA. It has been shown that this method, especially when dealing with large systems, strikes a compromise between computing efficiency and precision [52]. Molecular Mechanics/Generalized Born Surface Area (MM/GBSA) and Molecular Mechanics/Poisson-Boltzmann Surface Area (MM/PBSA) are arguably very popular methods for binding free energy prediction, being less computationally demanding than alchemical free energy methods and more accurate than most scoring functions of molecular docking. Gromacs trajectory and topology data were thus used along with the gmx_MMPBSA program to compute free energy. After creating an index file, the output was saved in the CSV (.csv) and DAT (.dat) formats. Using the gmx_MMPBSA ana module, the data listed in Tables 8–10 were examined. There are additional details regarding the receptor, ligand, and delta energy [53], these are shown in Fig. 17a, Fig. 17(b), and Fig. 17(c). Utilizing a Poisson-Boltzmann (PB) model, which is based on solving the Poisson-Boltzmann equation, MMPBSA is also a continuum solvation model [53]. From the (regression tests-2020) finalized result, the

Table 8
GMX_MMPBSA analyzed Parameters (Receptor).

GENERALIZED BORN					
Receptor	Average	SD (Prop.)	SD	SEM (prop.)	SEM
Energy Component (kcal/mol)					
BOND	9428005.48	2605938.29	2605938.29	1302969.14	1302969.14
ANGLE	1123.48	271.14	271.14	135.57	135.57
DIHED	309.37	5.77	5.77	2.89	2.89
UB	702895.53	455781.45	455781.45	227890.73	227890.73
IMP	229.90	334.40	334.40	167.20	167.20
CMAP	−95.82	0.79	0.79	0.40	0.40
VDWAALS	−382.01	9.62	9.62	4.81	4.81
EEL	−4061.47	61.61	61.61	30.81	30.81
1-4 VDW	164.78	3.23	3.23	1.61	1.61
1-4 EEL	2353.58	41.78	41.78	20.89	20.89
EPB	−1269.63	56.63	56.63	28.31	28.31
ENPOLAR	31.78	0.69	0.69	0.34	0.34
EDISPER	0.00	0.00	0.00	0.00	0.00
GGAS	10130539.34	2645496.41	2852811.31	1322748.21	1426405.66
GSOLV	−1237.85	56.63	55.98	28.32	27.99
TOTAL	10129301.49	2645496.41	2852770.99	1322748.21	1426385.49

Table 9
GMX_MMPBSA analyzed Parameters (Ligand).

GENERALIZED BORN					
Ligand	Average	SD (Prop.)	SD	SEM (prop.)	SEM
Energy Component (kcal/mol)					
BOND	3.48	1.47	1.47	0.74	0.74
ANGLE	15.67	1.61	1.61	0.81	0.81
DIHED	−2.95	1.31	1.31	0.66	0.66
UB	0.00	0.00	0.00	0.00	0.00
IMP	0.03	0.03	0.03	0.01	0.01
CMAP	0.00	0.00	0.00	0.00	0.00
VDWAALS	−0.13	0.36	0.36	0.18	0.18
EEL	5.30	1.22	1.22	0.61	0.61
1-4 VDW	4.70	0.57	0.57	0.29	0.29
1-4 EEL	−6.10	2.34	2.34	1.17	1.17
EPB	−7.65	0.52	0.52	0.26	0.26
ENPOLAR	1.98	0.02	0.02	0.01	0.01
EDISPER	0.00	0.00	0.00	0.00	0.00
GGAS	19.99	3.73	3.03	1.86	1.86
GSOLV	−5.67	0.52	0.51	0.51	0.26
TOTAL	14.32	3.77	3.00	1.88	1.50

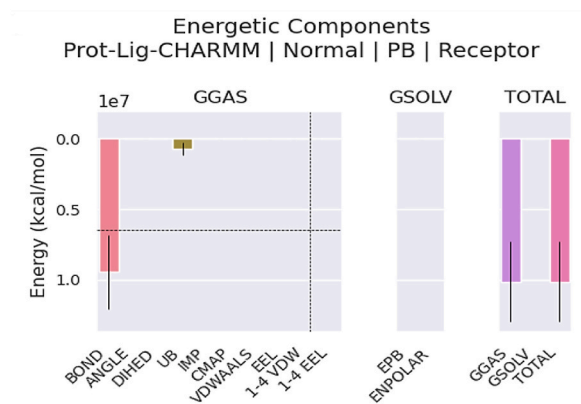confirmation of a non-broken bond is estimated along with the free energy.

4. Conclusion

Due to a negative correlation, the bond energy decreases as the bond length increases. This is due to the high electron density overlaps of the C–H bond and the low electron density overlap of the C–C bond. The hydrogen bonding's significant impact on transitions $n \rightarrow \sigma^*$ is confirmed through Absorption spectra. The lowering of the ppm value for C_3 is found in both the solvents and also confirms the hydrogen bonding with H–O ….H impression. With increasing bond strength and lowering decreased mass of the bound atoms, the value of the stretching frequency of a bond rises. The hydrogen atom is surrounded by high ELF areas, indicating a strong localization of both bonding and non-bonding electrons. The reduced density gradient reflects the interaction between van der Waals and is exhibited in colors and also portrays strong hydrogen bonds due to intermolecular interactions of 3,7-Dimethl-1,6-octadien-3-ol molecules. The radius of gyration gives the equilibrium confirmation of the entire system. The accuracy of the amino acid in protein reveals the molecular motion by the root mean square fluctuation. The average energy (short range) clearly states the protein-ligand interaction through hydrogen bond formation. From ADMET, ligands disclose the behavioral activity that can give access to function with protein interaction. The scoring function through the algorithm generates different poses and gives 50% of its binding during docking. From the regression tests through Molecular Dynamics confirmed the free energy of the protein-ligand interaction.

Table 10
GMX_MMPBSA analyzed Parameters -Delta (Complex - Receptor - Ligand).

GENERALIZED BORN: ((Delta (Complex - Receptor - Ligand))					
Delta	Average	SD (Prop.)	SD	SEM (prop.)	SEM
Energy Component (kcal/mol)					
ΔBOND	0.00	1.22	0.00	0.61	0.00
ΔANGLE	−0.00	0.96	0.00	0.48	0.00
ΔDIHED	−0.00	0.98	0.00	0.49	0.00
ΔUB	0.00	0.00	0.00	0.00	0.00
ΔIMP	−0.00	0.02	0.00	0.01	0.00
ΔCMAP	0.00	0.00	0.00	0.00	0.00
ΔVDWAALS	−14.04	1.01	2.07	0.51	1.03
ΔEEL	−1.28	0.84	0.22	0.42	0.11
Δ1-4 VDW	0.00	0.27	0.00	0.14	0.00
Δ1-4 EEL	−0.00	0.85	0.00	0.42	0.00
ΔEPB	5.12	0.20	0.92	0.10	0.46
ΔENPOLAR	−1.90	0.03	0.14	0.01	0.07
ΔEDISPER	0.00	0.00	0.00	0.00	0.00
ΔGGAS	−15.32	1.31	1.97	0.66	0.98
ΔGSOLV	3.22	0.20	0.85	0.10	0.43
ΔTOTAL	−12.10	1.33	1.42	0.66	0.71

ΔGbind, solv = ΔGbind, vacuum + ΔGsolv, complex, complex, complex− (ΔGsolv, ligand + ΔGsolv, receptor).

Fig. 17a. Gmx_mmpbsa energy of Receptor.
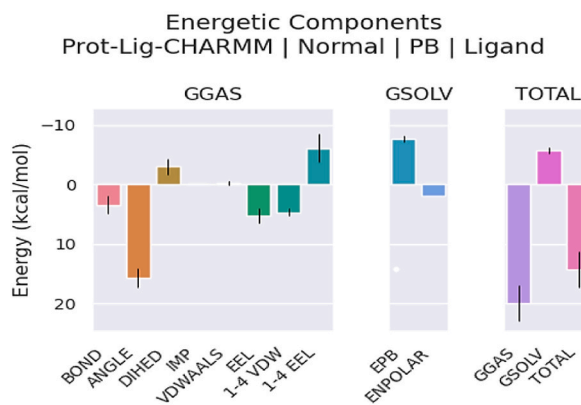
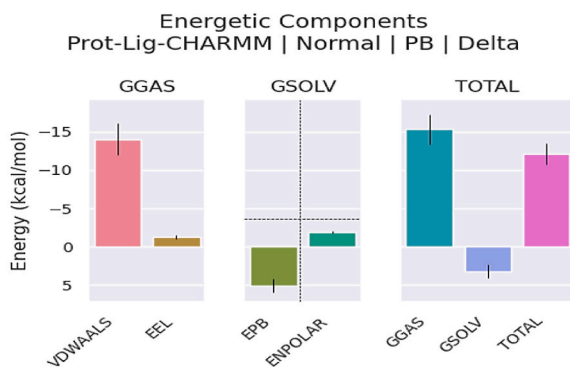**Fig. 17b.** Gmx_mmpbsa energy of Ligand.

Fig. 17c. Gmx_mmpbsa energy of Delta.

CRediT authorship contribution statement

Chandramohan Uma maheswari: Formal analysis, Writing – original draft, Validation, Investigation, Methodology, Writing – review & editing.

Declaration of competing interest

The authors declare that they have no known competing financial interests or personal relationships that could have appeared to influence the work reported in this paper.

References

[1] D.I. Sanchez-Vidaña, K.K.T. Po, T.K.H. Fung, J.K.W. Chow, W.K.W. Lau, P.K. So, B.W.M. Lau, H.W.H. Tsang, Lavender essential oil ameliorates depression-like behavior and increases neurogenesis and dendritic complexity in rats, Neurosci. Lett. 701 (2019) 180–192, https://doi.org/10.1016/j.neulet.2019.02.042.

[2] Éverton Renan Quaresma dos Santos, José Guilherme S. Maia, Enéas Andrade Fontes-Júnior, Cristiane do Socorro Ferraz Maia, Linalool as a therapeutic and medicinal tool in depression treatment: a review, Curr Neuropharmacology 20 (6) (2022) 1073–1092, https://doi.org/10.2174/1570159X19666210920094504.

[3] A.T. Peana, P.S. D Aquila, F. Panin, G. Serra, P. Pippia, M.D.L. Moretti, Anti-inflammatory activity of linalool and linalyl acetate constituents of essential oils, Phytomedicine 9 (2002) 721–726, https://doi.org/10.1078/094471102321621322.

[4] A.T. Peana, S. Marzocco, A. Popolo, A. Pinto, (−)-Linalool inhibits in vitro NO formation: probable involvement in the antinociceptive activity of this monoterpene compound, Life Sci. 78 (2006) 719–723, https://doi.org/10.1016/j.lfs.2005.05.065.

[5] A.T. Peana, P. Rubattu, G.G. Piga, S. Fumagalli, G. Boatto, P. Pippia, M.G. De Montis, Involvement of adenosine A1 and A2A receptors in (−)-linalool-induced antinociception, Life Sci. 78 (2006) 2471–2474, https://doi.org/10.1016/j.lfs.2005.10.025.

[6] P.P. Guy, Kamatou, Alvaro M. Viljoen, Linalool – a review of a biologically active compound of commercial importance, Nat. Prod. Commun. 3 (7) (2008) 1183–1192, https://doi.org/10.1177/1934578X080030072.

[7] Hizlan Hincal Agus, Chapter 4 - Terpene Toxicity and Oxidative Stress, Toxicology, Oxidative Stress and Dietary Antioxidants, Academic press, 2021, pp. 33–42, https://doi.org/10.1016/B978-0-12-819092-0.00004-2.

[8] Irina Pereira, Patrícia Severino, Ana C. Santos, Amélia M. Silva, Eliana B. Souto, Linalool bioactive properties and potential applicability in drug delivery systems, Colloids Surf. B Biointerfaces 171 (2018) 566–578, https://doi.org/10.1016/j.colsurfb.2018.08.001. ISSN 0927-7765.

[9] Ghaleb Al-Dahash, H.I. Abbood, Ghaidaa A. Hafed, Basim Abdullattif Ghalib, Theoretical study of geometry optimization and Energies for donor-π bridge-acceptor molecular system: B3LYP/DFT calculations, Int. J. ChemTech Res. 9 (10) (2016) 83–88. https://sphinxsai.com/2016/ch_vol9_no10/1/(83-89)V9N10CT.pdf.

[10] Ahmed M. Abu-Dief, M. Rafat, El-KhatibSynthesis, Faizah S. Aljohani, Hessah A. Al-Abdulkarim, Seraj Alzahrani, Gehad El-Sarrag, Mohamed Ismael, structural elucidation, DFT calculation, biological studies and DNA interaction of some aryl hydrazone Cr3+, Fe3+, and Cu2+ chelates, Comput. Biol. Chem. 97 (2022) 107643, https://doi.org/10.1016/j.compbiolchem.2022.107643.

[11] Gaussian 09, Revision A.02, M. J. Frisch, G. W. Trucks, H. B. Schlegel, G. E. Scuseria, M. A. Robb, J. R. Cheeseman, G. Scalmani, V. Barone, G. A. Petersson, H. Nakatsuji, X. Li, M. Caricato, A. Marenich, J. Bloino, B. G. Janesko, R. Gomperts, B. Mennucci, H. P. Hratchian, J. V. Ortiz, A. F. Izmaylov, J. L. Sonnenberg, D. Williams-Young, F. Ding, F. Lipparini, F. Egidi, J. Goings, B. Peng, A. Petrone, T. Henderson, D. Ranasinghe, V. G. Zakrzewski, J. Gao, N. Rega, G. Zheng, W. Liang, M. Hada, M. Ehara, K. Toyota, R. Fukuda, J. Hasegawa, M. Ishida, T. Nakajima, Y. Honda, O. Kitao, H. Nakai, T. Vreven, K. Throssell, J. A. Montgomery, Jr., J. E. Peralta, F. Ogliaro, M. Bearpark, J. J. Heyd, E. Brothers, K. N. Kudin, V. N. Staroverov, T. Keith, R. Kobayashi, J. Normand, K. Raghavachari, A. Rendell, J. C. Burant, S. S. Iyengar, J. Tomasi, M. Cossi, J. M. Millam, M. Klene, C. Adamo, R. Cammi, J. W. Ochterski, R. L. Martin, K. Morokuma, O. Farkas, J. B. Foresman, and D. J. Fox, Gaussian, Inc., Wallingford CT, 2016. https://gaussian.com/g09citation/..

[12] Kubra Sarikavak, Fatma Sevin, Structural and spectral (IR, NMR and UV/visible) properties of newly designed boronic acid derivatives containing DO3A sensitive to uranyl ion: a DFT and TD-DFT study, J. Comput. Chem. 5 (4) (2017), https://doi.org/10.4236/cc.2017.54012.

[13] Tian Lu, Feiwu Chen, Multiwfn, A multifunctional wavefunction analyzer, J. Comput. Chem. 33 (2012) 580–592, https://doi.org/10.1002/jcc.22885.

[14] Mark James Abraham, Teemu Murtolad, Schulzb Roland, Szilard Palla, C. Jeremy Smith, Berk Hessa, Erik Lindahl, GROMACS: high performance molecular simulations through multi-level parallelism from laptops to supercomputers, J. Softw. 1–2 (2015) 19–25, https://doi.org/10.1016/j.softx.2015.06.001.

[15] Hongbin Yang, Chaofeng Lou, Lixia Sun, Jie Li, Yingchun Cai, Zhuang Wang, Weihua Li, Guixia Liu, Yun Tang, admetSAR 2.0: web-service for prediction and optimization of chemical ADMET properties, Journal of Bioinformatics 35 (6) (2019) 1067–1069, https://doi.org/10.1093/bioinformatics/bty707.

[16] G.M. Morris, R. Huey, W. Lindstrom, M.F. Sanner, R.K. Belew, D.S. Goodsell, A.J. Olson, Autodock4 and AutoDockTools4: automated docking with selective receptor flexibility, J. Computational Chemistry 16 (2009) 2785–2791, https://doi.org/10.1002/jcc.21256.

[17] O. Trott, A.J. Olson, AutoDock Vina: improving the speed and accuracy of docking with a new scoring function, efficient optimization, and multithreading, J. Comput. Chem. (2010) 455–461, https://doi.org/10.1002/jcc.21334, 30, 31(2).

[18] M. Lundborg, Julimar, B. Hess, The accelerated weight histogram method for alchemical free energy calculations, J. Chem. Phys. 154 (2021) 204103, https://doi.org/10.1063/5.0044352.

[19] M. Benoit, D. Marx, The shapes of protons in hydrogen bonds depend on the bond length, ChemPhysChem 6 (2005) 1738–1741, https://doi.org/10.1002/cphc.200400533.

[20] Donald J. Pietrzyk, Clyde W. Frank, Qualitative Analysis: Ultraviolet, Visible, and Infrared, Analytical Chemistry, second ed., Academic Press, 1979, pp. 410–424, https://doi.org/10.1016/B978-0-12-555160-1.50022-8, 9780125551601.

[21] J. Uma Maheswari, S. Muthu, Tom Sundius QM/MM methodology, docking and spectroscopic (FT-IR/FT-Raman, NMR, UV) and Fukui function analysis on adrenergic agonist Spectrochimica, Acta Part A: Molecular and Biomolecular Spectroscopy 137 (2015) 841–855, https://doi.org/10.1016/j.saa.2014.07.095.

[22] DrS. Bakkialakshmi, S. Pushpa, Vibrational spectroscopy measurements of linalool with two flavonoids, International Journal of Creative Research Thoughts (IJCRT) 9 (2) (2021) 828–831. ISSN:2320-2882, https://ijcrt.org/papers/IJCRT2102103.pdf.

[23] H.D. Lutz, W. Eckers, H. Haeuseler, OH, stretching frequencies of solid hydroxides and of free OH− ions, J. Mol. Struct. 80 (1982) 221–224, https://doi.org/10.1016/0022-2860(82)87236-0.

[24] L.A. Parreira, A.F. Azevedo, L. Menini, E.V. Gusevskaya, Functionalization of the naturally occurring linalool and nerol by the palladium catalyzed oxidation of their trisubstituted olefinic bonds, J. Mol. Catal. Chem. 426 (2017) 429–434, https://doi.org/10.1016/j.molcata.2016.07.033.

[25] D. Lin-Vien, N.B. Colthup, W.G. Fateley, J.G. Grasselli, The Handbook of Infrared and Raman Characteristic Frequencies of Organic Molecules, Alkanes, 1991, pp. 9–28. eBook ISBN: 9780080571164,, https://www.sciencedirect.com/book/9780124511606/the-handbook-of-infrared-and-raman-characteristic-frequencies-of-organic-molecules.

[26] C. Uma Maheswari, S. Muthu, Sundius, tom, journal of result in chemistry, "combined quantum-mechanics/molecular-mechanics, molecular docking studies on hemorrhoid drug" 5 (2023) 100962, https://doi.org/10.1016/j.rechem.2023.100962.

[27] S. Maeda, Y. Harabuchi, Y. Ono, T. Taketsugu, K. Morokuma, Intrinsic reaction coordinate: calculation, bifurcation, and automated search, Int. J. Quant. Chem. 115 (2015) 258–269, https://doi.org/10.1002/qua.24757.

[28] Nadia Rega, Srinivasan S. Iyengar, Gregory A. Voth, H. Bernhard Schlegel, Thom Vreven, Michael J. Frisch, Hybrid ab-initio/empirical molecular dynamics: combining the ONIOM scheme with the atom-centered density matrix propagation (ADMP) approach, ACS Publication, Journal of Phys. Chem. B 108 (13) (2004) 4210–4220, https://doi.org/10.1021/jp0839829.

[29] Srinivasan S. Iyengar, H. Bernhard Schlegel, A. Gregory, Voth, atom-centered density matrix propagation (ADMP): generalizations using bohmian mechanics, ACS publication, Journal of Phys. Chem. A 107 (37) (2003) 7269–7277, https://doi.org/10.1021/jp034633m.

[30] Shuang Liu, Ma Yan-Zhen, Yang Yun-Fan, Liu Song-Song, Li Yong-Qing, Song Yu-Zhi, Excited state intramolecular proton transfer mechanism of o-hydroxy naphthyl phenanthroimidazole, Chin. Phys. B 27 (2) (2018) 023103, https://doi.org/10.1088/1674-1056/27/2/023103.

[31] S.B. Radder, Synthesis, spectroscopic (FT-IR, FT-Raman, NMR & UV-Vis), reactive (ELF, LOL, Fukui), drug-likeness and molecular docking insights on novel 4-[3-(3-methoxy-phenyl)-3-oxo-propenyl]-benzonitrile by experimental and computational methods, Journal of Helion 7 (11) (2021) e08429, https://doi.org/10.1016/j.heliyon.2021.e08429.

[32] Deepthi Joseph, Naiyf S. Alharbi, Ghulam Abbas, Muthu Sambantham, Vibrational spectra, effect of solvents in UV-visible, electronic properties, charge distribution, molecular interaction and Fukui analysis on 3-amino-2,5-dihydropyridine, Journal of De Gruyter (O) 10 (2023) 1515, https://doi.org/10.1515/zpch-2023-0462.

[33] Mouna Medimagh, Noureddine Issaoui, Sofian Gatfaoui, Aleksandr Kazachenko, Omar M. Al-Dossary, Naveen Kumar, Houda Marouani, Leda G. Bousiakoug, Investigations on the non-covalent interactions, drug-likeness, molecular docking and chemical properties of 1,1,4,7,7-pentamethyldiethylenetriammonium trinitrate by density-functional, J. King Saud Univ. Sci. 35 (2023) 102645, https://doi.org/10.1016/j.jksus.2023.102645.

[34] G. Venkatesh, S. Haseena, P. Vennila, Yudibeth Sixto-Lopez, V. Siva, J.N. Cheerlin Mishma, S. Abul Kalam Azad, Y. Sheena Mary, Solvation effects, structural, vibrational analysis, chemical reactivity, nanocages, ELF, LOL, docking and MD simulation on Sitagliptin (8) (2024) 100481, https://doi.org/10.1016/j.chphi.2024.100481.

[35] Sakshi Singh, Qanita Bani Baker, Dev Bukhsh Singh, Chapter 18 - molecular docking and molecular dynamics simulation, Journal of Bioinformatics Methods and Applications (2022) 291–304, https://doi.org/10.1016/B978-0-323-89775-4.00014-6.

[36] Steven M. Ryckbosch1, Paul A. Wender and Vijay S. Pande1, Molecular dynamics simulations reveal ligand-controlled positioning of a peripheral protein complex in membranes, Journal of Nature Communications, https://doi.org/10.1038/s41467-016-0015-8..

[37] Compchems.Com, How to run a Molecular Dynamics simulation using GROMACS, GROMACS basic functions and commands https://www.compchems.com/how-to-study-hydrogen-bonds-using-gromacs/#hydrogen-bonds-in-molecular-dynamics-simulations..

[38] William J. Allen, Justin A. Lemkul, David R. Bevan, Grid MAT-MD: a grid-based membrane analysis tool for use with molecular dynamics, Wiley Inter Science, J. Comput. Chem. 17 (2008) 1953–1958, https://doi.org/10.1002/jcc.21172.

[39] S.K. Paul, Molecular Modeling, molecular dynamics simulation, and essential dynamics analysis of grancalcin: an upregulated biomarker in experimental autoimmune encephalomyelitis mice, Journal of Helion 8 (10) (2022) e11232, https://doi.org/10.1016/j.heliyon.2022.e11232.

[40] H. Yang, W. Li, G. Liu, Y.J. Tang, ADMET-score - a comprehensive scoring function for evaluation of chemical drug-likeness, Journal of MedChemComm 1 (10) (2019) 148–157, https://doi.org/10.1039/c8md00472b.

[41] H. Krishna Kishor, S A Hitesh, Navneet Karanth, Admet Biological Activity Prediction and Docking Studies of Main Phytoconstituents Present in Eucalyptus Using Computational Tools, International Journal of Innovative Science and Research Technology, https://doi.org/10.21203/rs.3.rs-2480381/v1..

[42] Hongbin Yang, Lixia Sun, Zhuang Wang, Weihua Li, Guixia Liu, Yun Tang, ADMET opt: a web server for ADMET optimization in drug design via scaffold hopping, ACS Publication Journal of Chem. Inf. Model. 58 (10) (2018) 2051–2056, https://doi.org/10.1021/acs.jcim.8b00532.

[43] Abdellatif Rafik, Burak Tüzün, Hafid Zouihri, Lahcen EL Ammari, Zaki S. Safi, Nuha A. Wazzan, Taufiq Guedira, Crystal growth, morphological, mechanical, spectroscopic studies, optical properties, molecular docking, ADME/T, Hirshfeld surfaces analysis and theoretical calculations of hybrid organic-inorganic phosphate compound 111828 (160) (2024), https://doi.org/10.1016/j.inoche.2023.111828.

[44] N. Mani, S. Suresh b, M. Govind Ammal, S. Kannan, E. Isac Paulraj, D. Nicksonsebastin, M. Prasath, Spectroscopic (FT-IR, FT-Raman, NMR and UV–visible), ADMET and molecular docking investigation of aztreonam as anti-tuberculosis agent 7 (2023) 100254, https://doi.org/10.1016/j.chphi.2023.100254.

[45] Sakshi Singh, Qanita Bani Baker, Dev Bukhsh Singh, Chapter 18 - molecular docking and molecular dynamics simulation, Journal of Bioinformatics Methods and Applications (2022) 291–304, https://doi.org/10.1016/B978-0-323-89775-4.00014-6.

[46] Necmi Dege, Ömer Tamer, Merve Şimşek, Mavişe Yaman, Başoğlu Adil, Yusuf Atalay, Experimental and Theoretical Approaches on Structural, Spectroscopic (FT-IR and UV-Vis), Nonlinear Optical, and Molecular Docking Analyses for Zn (II) and Cu (II) Complexes of 6-Chloropyridine-2-Carboxylic Acid, vol. 10, 2022, p. 1002, https://doi.org/10.1002/aoc.6678.

[47] G. Morris, D. Goodsell, R. Halliday, R. Huey, W. Hart, R. Belew, A.J. Olson, Automated docking using a Lamarckian genetic algorithm and an empirical binding free energy function, J. Comput. Chem. 19 (1998) 1639–1662, https://doi.org/10.1002/(SICI)1096-987X(19981115)19:14%3C1639::AID-JCC10%3E3.0.CO;2-B.

[48] BIOVIA, Dassault Systems, [Discovery Studio Visualizer], [Discovery Studio 2021 Client], Dassault Systems, San Diego, 2021. https://3ds.com/products-services/biovia/products.

[49] S. Asokan, S. Sebastian, B. Karthikeyan, S. Xavier, R. Ganapathi Raman, S. Silvan, S. Sangeetha Margreat, R. Sagayaraj, Exploring Molecular Structure (Monomer & Dimer), Spectroscopic (FT-IR, FT-Raman, UV-Vis, NMR), TG/DTA, Antibacterial and Molecular Docking Investigation on 2-[2,3-Dichloro-4-(2-Methylide-nebutanoyl)phenoxy] Acetic Acid by DFT and Wavefunction Analysis, Chemical Physics Impact 8 (2024) 100497, https://doi.org/10.1016/j.chphi.2024.100497.

[50] Chandramohan Uma Maheswari, Computational biology of antibody epitope, tunnels and pores analysis of protein glutathione S-transferase P, and quantum mechanics, Journal of Biochemistry and Biophysics Reports 36 (2023) 101581, https://doi.org/10.1016/j.bbrep.2023.101581.

[51] Shiyu Wang, Xiaolin Sun, Wenliang Cui, Shuguang Yuan, MM/PB(GB)SA benchmarks on soluble proteins and membrane proteins, Journal of Front. Pharmacol., Sec. Pharmacology of Anti-Cancer Drugs (2022) 13, https://doi.org/10.3389/fphar.2022.1018351.

[52] Mario S. Valdés-Tresanco, Mario E. Valdés-Tresanco, Pedro A. Valiente, Ernesto Moreno, gmx_MMPBSA: a new tool to perform end-state free energy calculations with GROMACS, J. Chem. Theor. Comput. 17 (10) (2021) 6281–6291, https://doi.org/10.1021/acs.jctc.1c00645.

[53] Yasir Muhammad, Jin Young Park, Yuno Lee, Yong Soo Kwon, Hee Jae Lee, Wanjoo Chun, Computational exploration of the effects of mutations on GABA aminotransferase in GABA aminotransferase deficiency, Int. J. Mol. Sci. 24 (13) (2023) 10933, https://doi.org/10.3390/ijms241310933.